EXPERIMENTAL AND NUMERICAL STUDIES ON LEAN TURBULENT PREMIXED FLAMES

A THESIS SUBMITTED TO
THE GRADUATE SCHOOL OF NATURAL AND APPLIED SCIENCES
OF
MIDDLE EAST TECHNICAL UNIVERSITY

BY

DİLAY GÜLERYÜZ

IN PARTIAL FULFILLMENT OF THE REQUIREMENTS
FOR
THE DEGREE OF MASTER OF SCIENCE
IN
MECHANICAL ENGINEERING

AUGUST 2023

Approval of the thesis:

EXPERIMENTAL AND NUMERICAL STUDIES ON LEAN TURBULENT PREMIXED FLAMES

submitted by **DİLAY GÜLERYÜZ** in partial fulfillment of the requirements for the degree of **Master of Science** i**n Mechanical Engineering, Middle East Technical University** by,

Prof. Dr. Halil Kalıpçılar
Dean, Graduate School of **Natural and Applied Sciences** _____

Prof. Dr. Sahir Arıkan
Head of the Department, **Mechanical Engineering** _____

Prof. Dr. Ahmet Yozgatlıgil
Supervisor, **Mechanical Engineering, METU** _____

Prof. Dr. İskender Gökalp
Co-Supervisor, **TÜBİTAK Marmara Research Center** _____

Examining Committee Members:

Assoc. Prof. Dr. Hüsnü Dal
Mechanical Eng, METU _____

Prof. Dr. Ahmet Yozgatlıgil
Mechanical Eng., METU _____

Asst. Prof. Dr. Özgür Uğraş Baran
Mechanical Eng., METU _____

Assoc. Prof. Dr. Feyza Kazanç Özerinç
Mechanical Eng., METU _____

Prof. Dr. Metin Muradoğlu
Mechanical Eng., Koç University _____

Date: 08.08.2023

I hereby declare that all information in this document has been obtained and presented in accordance with academic rules and ethical conduct. I also declare that, as required by these rules and conduct, I have fully cited and referenced all material and results that are not original to this work.

Name Surname: Dilay Güleryüz

Signature :

ABSTRACT

EXPERIMENTAL AND NUMERICAL STUDIES ON LEAN TURBULENT PREMIXED FLAMES

Güleryüz, Dilay
Master of Science, Mechanical Engineering
Supervisor: Prof. Dr. Ahmet Yozgatlıgil
Co-Supervisor: Prof. Dr. İskender Gökalp

August 2023, 88 pages

Combustion emissions mitigation requirements and increased energy efficiency demands pose stringent conditions on the design of new combustors. Emission requirements indicate the use of hydrogen (as fuel and energy carrier) as a potential solution. Although hydrogen decreases carbon emissions when substituted with carbon-based fuels, it has many peculiarities, such as higher flame propagation velocities, reduced instantaneous flame thickness, increased flame flashback risks, reduced average flame dimensions, increased flame temperature, and increased NO_x emissions potential due to higher flame temperatures. These characteristics justify the detailed investigation of hydrogenated mixtures.

Another way to reach efficient and cleaner combustion is to use lean premixed fuels.. However, lean premixed combustion faces the problem of flame instability; therefore, predicting the design points in terms of flame properties is crucial for better combustor designs.

The experimental facility we developed permits such investigations. The system comprises a high pressure combustion chamber, a turbulent premixed flame burner.

The optical diagnostics used are OH* and CH* chemiluminescence and laser induced Mie Scattering tomography technics.

Turbulent lean premixed flames under atmospheric pressure for various hydrogen + natural gas + air mixtures are experimentally and numerically investigated. The main premixed turbulent flame parameters we determined concern the instantaneous and average flame topology (such as the turbulent flame brush thickness, flame height, and flame curvature distributions) from which we deduced global combustion parameters such as the turbulent flame propagation speed. In addition, Large Eddy Simulation computations by employing various calculation methods are performed. The numerical results are compared with the experiments.

Keywords: Combustion, Lean Premixed Turbulent Flames, Hydrogen, Optical Measurement Techniques, CFD

ÖZ

FAKİR ÖNKARIŞIMLI TÜRBÜLANSLI ALEVLERİN DENEYSEL VE NÜMERİK OLARAK İNCELENMESİ

Güleryüz, Dilay
Yüksek Lisans, Makina Mühendisliği
Tez Yöneticisi: Prof. Dr. Ahmet Yozgatlıgil
Ortak Tez Yöneticisi: Prof. Dr. İskender Gökalp

Ağustos 2023, 88 sayfa

Artan enerji verimliliği ve yanma ürünü olan emisyonların azaltılması talepleri, yakıcı tasarımlarında katı gereksinimler oluşturmaktadır. Emisyon azaltma zorunluluğu, bir çözüm olarak hidrojenin (yakıt ve enerji taşıyıcısı olarak) kullanılabileceğini işaret etmektedir. Hidrojen, karbon bazlı yakıtlara ilave edildiğinde karbon emisyonlarını azaltsa da, yüksek alev yayılma hızları, azalan ani alev kalınlığı, artan alev geri tepme riskleri, azalan ortalama alev boyutları, artan alev sıcaklığı ve sıcaklığa bağlı olarak artan NO_x emisyon potansiyeli gibi birçok olumsuz etkisi de bulunmaktadır. Bu özellikler, geleceğin yakıtı olarak hidrojen karışımlarının ayrıntılı araştırmasını gerekli kılmaktadır.

Fakir önkarışımlı alevlerin uygulamaları verimli ve temiz yanma için kullanılabilecek bir diğer yöntemdir. Bununla birlikte, bu yanma koşulları alev kararsızlığı sorununu ortaya çıkarmaktadır; bu nedenle, tasarım noktalarının alev özellikleri açısından tahmin edilmesi son derece önemlidir.

Geliştirdiğimiz deney düzeneği bu tür araştırmaların yapılmasına olanak sağlamaktadır. Deney düzeneğinin ana elemanları yüksek basınçlı yanma odası ve ,

ön karışımlı Bunsen tipi türbülanslı yakıcıdır. Bu tezde esas olarak OH* ve CH* kemilüminesans ve lazer kaynaklı Mie Saçılma tekniklerini kullandık.

Çeşitli karışım bileşimleri (eşdeğerlik değerleri) ve hidrojen katma oranlarına sahip doğalgaz-hava önkarışımlı yakıtlar kullanılarak atmosferik basınç altında türbülanslı yakıt-fakir alevler için deneyler ve sayısal hesaplamalar yapılmıştır. Deneysel çalışmalar sayesinde alevlerin anlık topolojileri (anlık alevlerin zamansal ve mekansal dinamiği, anlık alev kıvrımlarının istatistiksel dağılımı) belirlenmiş ve bu değerler kullanılarak alevin ortalama parametrelerine ulaşılmıştır (alev ortalama yüksekliği, alevin ortalama kalınlığı, türbülanslı alevin ilerleme hızı). Deneysel çalışmalara paralel olarak yapılan sayısal benzetimlerde, Büyük Girdap Simülasyonu (Large Eddy Simulation) hesaplamaları yapılmış ve elde edilen alev ortalama özellikleri deneysel verilerle karşılaştırılmıştır.

Anahtar Kelimeler: Yanma, Türbülanslı Fakir Önkarışımlı Alevler, Hidrojen, Optik Ölçüm Teknikleri, HAD

To my family

ACKNOWLEDGMENTS

I want to express my deepest gratitude to Prof. Dr. İskender Gökalp for his invaluable guidance, availability, and attention. It is truly an honor and privilege to be his student. I extend my thanks to Ahmet Yozgatlıgil for the opportunity to work with him.

I express my heartfelt thanks to Dr. Christophe Allouis, for his support, guidance, and encouragement. I thank Dr. Mehmet Karaca for his guidance in the numerical aspect of this work. I express my thanks to Dr. Barış Yılmaz for his suggestions and comments.

I am sincerely thankful to all members of my jury for their valuable comments and time.

This work is fully funded by the Scientific and Technological Research Council of Turkey (TÜBİTAK) under grant number TUBİTAK 118C287, a project of the program BIDEB2232-A International Fellowship for Outstanding Researchers. I would like to thank TÜBİTAK for the master scholarship grant, and the financial support to conduct my research for the scope of the thesis.

I would like to thank TÜBİTAK SAGE for allowing me to conduct my experimental work in their facilities, with a special acknowledgment to Semra Gümrük Tokgöz for her exceptional support. I am grateful to TÜBİTAK ULAKBİM for granting me access to the national supercomputing network.

I extend my thanks to my esteemed friend, Berk Kıymaz, for his dear friendship, particularly during challenging times. Additionally, I thank Emre Böncü for his valuable comments and encouragement.

I am deeply grateful to my family, my mom, my dad, and my sister for their endless love. Thank you for always believing in me and supporting me through my whole life. My cousin Miray, thank you for your endless love and faith in me. My uncle

Habil, thank you for your constant inspiration and for always being there for me. I thank my dear friend Utku, for always cheering me up when I need the most. Lastly, I extend my heartfelt appreciation to Canberk for his unwavering patience, understanding, and the joy he brings into my life.

TABLE OF CONTENTS

LIST OF TABLES

TABLES

LIST OF FIGURES

FIGURES

LIST OF ABBREVIATIONS

CFD	Computational Fluid Dynamics
HC	Hydrocarbons
ICE	Internal Combustion Engine
LES	Large Eddy Simulation
DNS	Direct Numerical Simulation
RANS	Reynolds Averaged Navier-Stokes
BML	Bray-Moss-Libby model
FSD	Flame Surface Density
ASFW	Algebraic Flame Surface Wrinkling
MIE	Mie Scattering
CL	Chemiluminescence
NG	Natural Gas
RMS	Root Mean Square
XI	XiFoam
PDF	Probability Density Function

LIST OF SYMBOLS

$\boldsymbol{v_u}$	Unburned viscosity
S	Flame propagation speed
$\boldsymbol{n}$	Flame front normal vector
κ	Flame Stretch
A	Geometric Cross Section of Total Flame Surface
A_T	Total Flame Surface Area
t	Time
Y	Mass fraction
ϕ	Equivalence ratio
r	Curvature radius
$\bar{\boldsymbol{u}}$	Mean velocity vector
$\boldsymbol{u}'$	Fluctuating velocity vector
u_{rms}	Root-mean-square velocity
L	Integral length scale
τ	Integral time scale
η	Kolmogorov length scale
τ_η	Kolmogorov time scale
υ_η	Kolmogorov velocity scale
ν	Kinematic viscosity
ε	Turbulent kinetic energy dissipation rate
D	Diffusivity
S_L	Laminar burning velocity
Da	Damköhler number
Ka	Karlovitz number
τ_C	Chemical Time Scale
τ_F	Flow Time Scale
Ξ	Wrinkling Factor

T	Temperature
W	Molar weight
ρ	Density
τ_{ij}	Viscous stress tensor
P	Pressure
μ	Dynamic viscosity
δ_{ij}	Kronecker delta
c	Progress variable
c_p	Constant pressure specific heat
λ	Wavelength of laser
d	Scattering Particle Diameter
κ	Curvature
ψ	Slope angle
r	Radius of the circle
h_s	Sensible enthalpy
$\dot{Q}$	Heat Source
q	Heat Flux
$\dot{\omega}_T$	Heat Produced by Combustion
F	LES Filter
$\tilde{f}$	Favre Filtered Quantity
Sc_t	Turbulent Schmidt number
Δ	Filter size
δ_L	Laminar flame thickness
k	SGS kinetic energy
S_{ij}	Strain tensor

CHAPTER 1

INTRODUCTION

Combustion for heat and power generation has always been an essential and intriguing topic for mankind. It may be defined as an oxidation procedure that generally produces heat and light from various kinds of fuels. Combustion research is essentially a synthesis of thermodynamics, heat transfer, molecular transport of heat and mass, chemical kinetics, and fluid mechanics.

Today, many energy technologies, from common everyday domestic appliances to advanced transport and propulsion devices, primarily depend on combustion applications. The electricity we use primarily depends on combustion as well.

Fossil fuels still make up the majority of the world's electricity generation resources, producing 61% of it in 2022. For the same year, 36% of the world's electricity generation originated from coal, 22% from natural gas, and 3% from other fossil fuels [1]. Electricity generation in Türkiye too still depends for 45% on burning natural gas and coal.

While electricity generation is a major topic in everyday human life, industrial processes, transport, and aerospace applications also heavily depend on combustion technologies. Combustion of carbon containing fossil fuels inevitably produces many emissions, harmful to environment and to human health. Combustion of hydrocarbon fuels produces CO_2, unburnt or partially burnt hydrocarbons, NO_x, CO, and SO_x emissions. Different engines produce different hazardous products; for example, a spark ignition engine may produce unburnt HC's, NO_x, and CO; while gas turbine engines, together with internal combustion engines, also produce particulate matter. Coal-burning utility boilers are major producers of SO_x emissions,

the main cause of world acid rains [2]. The current regulations on carbon emissions place heavy burdens on combustion technologies and drive the combustion research to create more carbon-neutral solutions without losing efficiency during the energy generation process.

There are two main types of flame modes, which are premixed and non-premixed flames. For premixed flames the fuel and the oxidizer are mixed at the molecular level before combustion happens. The non-premixed mode corresponds to the flame mode where the fuel and oxidizer enter the burner in separate streams and are mixed during the combustion process. Both flame types may happen in laminar and turbulent flame motions. Examples include gas turbines and spark ignited ICEs for premixed turbulent flames, and aviation engines, rocket motors, and diesel engines for non-premixed turbulent flames [3].

The scope of the thesis covers turbulent premixed combustion, which usually takes place within high-pressure environments. Considering the emission regulations, the combustion R&D is forced forward burning HC fuels in leaner conditions and the utilization of hydrogen or hydrogenated mixtures to decrease CO_2 and NO_x emissions; therefore, it is crucial to study the effect of burning hydrogenated mixtures in various combustion configurations [4, 5].

1.1 Motivation and Problem Definition

Experimental and numerical investigations of lean turbulent premixed flames of hydrogenated mixtures are the main objective of this thesis. The validation results of the newly installed combustion chamber, and the turbulent Bunsen burner operating with natural gas-hydrogen-air premixtures under lean conditions are presented in the scope of the thesis. The results only concern atmospheric pressure conditions.

1.2 Methods

A high-pressure combustion chamber including a turbulent Bunsen burner is designed and built, together with a premixing system. For the computational part of the study, the Large Eddy Simulation (LES) approach is used. The details of the experimental setup and the chemiluminescence and the laser induced Mie scattering tomography data from the experiments are presented and discussed. The experimental results are used for determining the effects of hydrogen addition to the reactive mixture in terms of various combustion and flame parameters. Experimental results are also used to validate the computational approach.

1.3 Contribution and Novelties

During this thesis, a general purpose optically accessible high-pressure combustion chamber for turbulent premixed flame studies is designed and built. The system allows studies with several burner configurations in a high pressure environment. For the present thesis, only atmospheric pressure experiments were performed.

The experimental setup can be used with various fuel mixtures and for varying turbulence properties. For the numerical simulation part of the study, the OpenFoam XiFoam solver is adapted for turbulent premixed flames with various hydrogen addition rates and equivalence ratios. creating a comparison matrix to investigate the effects of hydrogen addition on the combustion of turbulent premixed natural gas – air flames.

1.4 Outline of the Thesis

The thesis covers the investigation of lean turbulent premixed Bunsen type flames experimentally and numerically. The thesis is composed of 5 chapters.

• Following this introductory one, Chapter 2 introduces lean turbulent premixed flames research, by covering their investigation methods both experimentally and

numerically through a literature survey. Laminar and turbulent flames are adressed by defining the fundamental parameters.

• Chapter 3 presents the experimental and numerical methodologiesused in this thesis. The newly built high pressure combustion chamber with the turbulent Bunsen burner is presented. The used numerical methods are presented. The postprocessing methods for both the experimental and numerical approaches are explained.

• Chapter 4 presents the experimental and numerical results on lean turbulent premixed flames for various equivalence ratios and hydrogen addition rates. Eexperimental results are first presented, followed by the validation of the numerical results by the experiments.

• Chapter 5 concerns the conclusions and future work suggestions for the investigation of turbulent lean premixed hydrogenated flames.

CHAPTER 2

LITERATURE REVIEW

In this literature review chapter, the turbulent premixed combustion phenomena, the experimental and numerical methods to study turbulent premixed flames are briefly discussed and previous work related to the topics are presented. Emphasis is given on the methods used in the thesis, such as large eddy simulations with G-Equation, chemiluminescence, and laser induced Mie scattering measurement techniques.

2.1 Turbulent Premixed Combustion

Fuel and oxidizer must be mixed at the molecular level prior to ignition to create a premixed flame. Premixed turbulent combustion is widely used in industrial applications. Examples include spark-ignition engines, jet engines with premixing and pre-vaporization, and industrial process burners.

If the flame is laminar and premixed, the chemical combustion processes depend essentially on the mixture composition and its temperature and pressure. When the flame is turbulent and premixed, the corrugations and distortions of the instantaneous flame surface affect the molecular transport processes and turbulent mixing between the hot and cold gases as well as the transport of active chemical species (such as the radical species) become the dominant processes [6].

Turbulent premixed flames can be typically represented as instantaneous laminar flames (called often flamelets) fluctuating in space and time by following the turbulence characteristics of the cold premixture. The challenge for turbulent premixed flame research is therefore essentially to relate the cold flow turbulence characteristics to the spatio-temporal dynamics of instantaneous flame fronts.

Compared to a laminar flame of the same reactive mixture, such flame front movements or wrinkles allow increasing the flame surface area in a unit volume and hence increase the burning rate.

The turbulent premixed flames are generally defined by analogy to laminar flames in terms of the flame propagation velocity, flame thickness and characteristic chemical time [7].

The flame thickness δ_L, the flame speed S_L and the time scale $\tau_F = \delta_L/S_L$are three measurable characteristics of laminar flames. Following the representation of a turbulent flame as a collection of wrinkled laminar flames, we first divide the turbulent scales into a range of eddy sizes, the limits being the smallest and largest eddies. The biggest eddies are those with the largest values of the integral length scale L, integral time scale $\tau = L/u'$, and root mean square (rms) turbulent velocity u'. The smallest eddies include the Kolmogorov velocity u_η, Kolmogorov length scale η, and the Kolmogorov time scale τ_η. Kolmogorov turbulence theory states that [8]:

$$u_\eta \propto u' Re_T^{-1/4} \ll u' \tag{2.1}$$

$$\tau_\eta \propto \tau_T Re_T^{-1/2} \ll \tau_T \tag{2.2}$$

$$\eta \propto L\, Re_T^{-3/4} \ll L \tag{2.3}$$

with the turbulent Reynolds number Re_T defined as [6].

$$Re_T = u'L/\nu_u \gg 1 \tag{2.4}$$

where ν_u is the unburned reactants kinematic viscosity.

The research on turbulent premixed flames goes back to the work of Damköhler in the 1940ies on turbulent premixed flames [9] Damköhler stated that whereas sufficiently small-scale turbulence primarily influences the transport processes within the instantaneous flame front, large-scale turbulence just wrinkles the premixed laminar flame without significantly changing its internal structure. Thus,

two limiting regimes were suggested in which, together with the thickness of a laminar flame, turbulence scales play an important role.

Following Damköhler's work, premixed turbulent combustion studies progressed in terms of flame – turbulence interactions analyzing the relations between the characteristic scales related to the laminar flames and to the turbulence structure. The main characteristic scales used are presented below where ε is the turbulence dissipation rate [10].

$$u_\eta = (\nu\,\varepsilon)^{\frac{1}{4}} = u' Re_T^{-1/4} \tag{2.5}$$

$$\tau_\eta = (\nu\,\varepsilon)^{1/2} = \tau Re_T^{-1/2} \tag{2.6}$$

$$\eta = (\nu^3\varepsilon)^{\frac{1}{4}} = L\,Re_T^{-3/4} \tag{2.7}$$

$$\varepsilon = u'^3/L \tag{2.8}$$

and

$$\eta = (\nu^3/\varepsilon)^{1/4} \tag{2.9}$$

$$\tau_\eta = (\nu/\varepsilon)^{1/2} \tag{2.10}$$

$$u_\eta = (\nu\varepsilon)^{1/4} \tag{2.11}$$

Together with the turbulent Reynold number Re_T, other non-dimensional parameters are also introduced. One is the Karlovitz number Ka which is the ratio between the flame and Kolmogorov time scales. The Damköhler number introduces the ratio between the turbulence integral time scale and the flame time scale. The following relations show how these parameters are related to each other [10]:

$$Ka = \frac{\tau_C}{\tau_\eta} = \left(\frac{\delta_L}{\eta_\eta}\right)^2 = \left(\frac{u_\eta}{S_L}\right)^2 = \left(\frac{u'}{S_L}\right)^{\frac{3}{2}}\left(\frac{L}{\delta_L}\right)^{-1/2} = \left(\frac{\varepsilon\,\delta_L}{S_L^3}\right)^{1/2} = \left(\frac{u'}{S_L}\right)^2 Re_T^{-1/2} = \frac{Re_T^{1/2}}{Da} \tag{2.12}$$

$$Da = \frac{\tau_F}{\tau_C} \tag{2.13}$$

$$Re_T = Da^2 Ka^2 \tag{2.14}$$

In these equations, the $\delta_L = \nu_u / S_L$ relation is also employed.

One classical approach to identify the various turbulent combustion regimes is using regime diagrams based on the previous parameters, based on the initial limiting regimes classification by Damköhler [9].

The first turbulent premixed flame regime occurs when all turbulence length scales are smaller than the laminar flame thickness. This regime is called the "distributed reaction zone" regime. The second limiting regime occurs when all turbulence length scales are larger than the laminar flame thickness. This regime is called the "wrinkled flame regime". In between these two limiting regimes there are several intermediary or hybrid ones represented on the following regime diagrams.

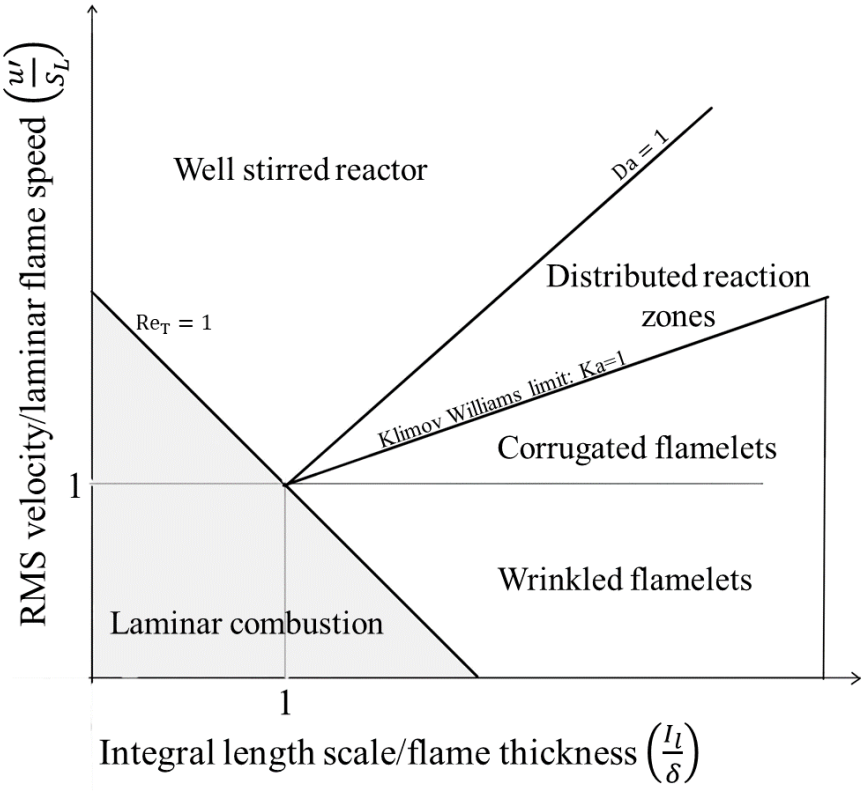

Figure 2.1. Classical turbulent combustion regime diagram [11]

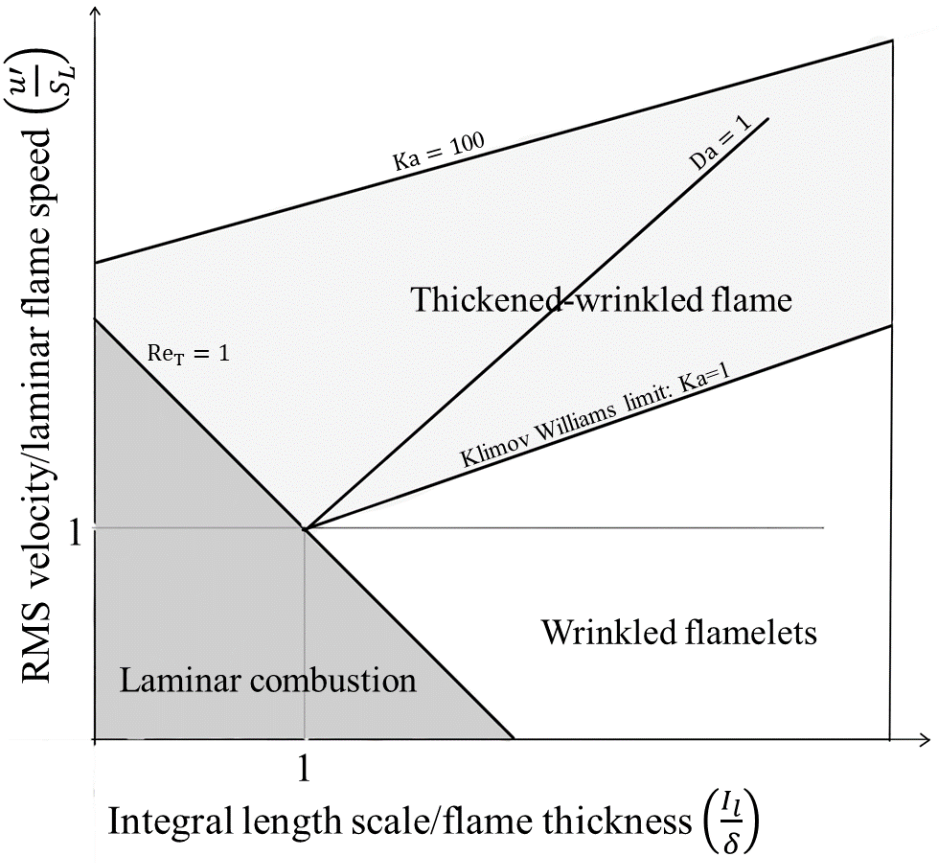

Figure 2.2. Modified turbulent combustion regime diagram [12]

The turbulent flame speed S_T is another crucial characteristic of turbulent premixed flames. An easy way to define S_T is to refer to it as a mass flux per area. The area should be chosen as the surface of the time-averaged flame zone, but the location of this zone is very crucial. The inner or outer selections have a significant effect on the S_T values.

;The following are some general characteristics established for S_T:

1. In all cases, S_T is greater than S_L (the laminar flame speed).
2. S_T increases with increasing turbulence in the cold premixture.

3. The response of S_T to the cold flow turbulence may vary depending on whether the flame is confined or unconfined.

Unlike the laminar flame speed S_L, which can be easily defined and measured and is a characteristic property of the reactive mixture alone, S_T is not an easily measurable quantify and one must use certain assumptions to calculate it [13,14]. There are several propositions of correlations to calculate the turbulent flame speed. S_T as an eigenvalue like the laminar flame speed problem. The first proposal goes again back to Damköhler who proposed:

$$S_T = S_L + u' \tag{2.15}$$

Later Karlovitz et al. [15] proposed the flame-generated turbulence concept to extend the turbulent flame speed definition.

The present correlations of S_T typically follow Damköhler's proposal in the following form: [16]:

$$\frac{S_T}{S_L} = A + B\frac{u_0'}{S_L} \tag{2.16}$$

where A and B depend heavily on the turbulent Reynolds number [6].

2.2 Numerical Methods for Investigating Turbulent Premixed Flames

Numerical simulations allow researchers to investigate the complex dynamics of turbulent premixed flames, providing insights into their behavior, stability, and pollutant emissions. Numerical simulations are very useful for investigating flames as experiments can be cumbersome in terms of preparation, budget, and especially optical access to the flame. Numerical simulations allow the user to investigate flame properties which are not easy to capture in experiments, such as flame thickness or 3D topography.

For the numerical investigations of turbulent premixed flames, the first approach is phenomenological, such as the modeling of the flame wrinkling effect by turbulence. Flame wrinkling can be modeled by the wrinkling factor, $\Xi = A_T/A$ where A_T is the total flame surface and the A is its geometric cross-section. This correlation is useful to define the turbulent flame speed S_T as well, since as the A_T/A ratio also represents S_T/S_L.

In a turbulent premixed flame, the flame front and turbulence continuously influence and modify each other. These effects include the changes in local Reynolds number, kinematic viscosity, density, buoyancy, and temperature, between the reactants and products. The flame also accelerates through the flame front; therefore, velocity field also changes. The modeling approach including all these effects is to model the turbulent premixed flame as a two-state flow of unburned and burnt states.

Turbulent premixed flames are investigated with three types of numerical approaches, which are the Reynolds Averaged Navier Stokes Simulations (RANS), Large Eddy Simulations (LES), and Direct Numerical Simulations (DNS). The computational costs are the highest for DNS and lowest for RANS.

For RANS calculations of turbulent premixed flames, various simulation strategies are employed for practical combustion simulations. The first is the use of single-step chemistry, where the simulations use only one global irreversible chemical reaction. In this case, unity Lewis number and constant pressure are assumed, and only two states of the flow, of the reactants and the products, are modeled. The second model is the no-model (Arrhenius) approach. In this model, the effects of turbulence are ignored. The limitation of this model is that it is only applicable in the well-stirred reactor regime or the distributed reaction zone regime, where the mixing is rapid but burning is slow. Examples include supersonic combustion and chemical reactions in atmospheric boundary layers [10]. The opposite of the no-model approach is the eddy breakup model of Spalding [17], where the Reynolds and Damköhler numbers are both large. This model does not consider chemistry effects and assumes that the controlling mechanism for the reaction rate is turbulence, meaning “mixed is

burned". Another way to describe turbulent premixed flames in RANS simulations is the G-Equation model. The G-Equation describes the propagation of the flame front, while the turbulent flame speed is modeled according to some correlations. The G-Equation models are both applicable to RANS and LES models. Bray et al. [18] proposed the infinitely thin flame front model as a tool to investigate turbulent premixed flames. The model is known as the Bray Moss-Libby model (BML), where the reduced temperature is represented by two limiting states, 0 in fresh gases and 1 in burnt gases. The model employs probability density functions combined with physical analysis. The mean reaction rate is computed based on the flame surface area in flame surface density models. The model is valid in the flamelet regime, and its biggest advantage is separating the chemical reactions from turbulence-combustion interactions. The last model is the probability density function (pdf) model which is applicable in all regimes of the turbulent premixed combustion diagram. The model represents the probability density function of the reduced temperature with two options; the first is the presumed pdf approach and the second is to solve a balance equation for the pdf.

LES is a useful tool to investigate transient flows with higher resolution, but it carries certain problems when applied to turbulent premixed combustion where the flame front is very thin (of the order of 0.1 to 1 mm for most flames). The mesh size could fail to resolve the combustion front for all simulations. That is why three models have been produced to overcome the difficulty to solve the turbulent premixed flame with LES. The first model is the artificially thickened flame front in which the flame is thickened by a certain coefficient F, allowing it to be resolved by current mesh resolution [19]. The second model is the G-Equation approach. The equation tracks the flame front but is directly the opposite of the thickened flame approach. This model assumes the flame front thickness as zero and describes the flame front as a moving surface. The problem of the model is that it should assume a subgrid formulation for turbulent flame speed, which is not a well-defined quantity to this day. The final model is the formulation of flame surface density for LES [20]. For the progress variable (or the mass fraction), the model utilizes a filtered balance

equation; the variable is generally resolvable in the LES mesh. The main advantage of this approach is that the progress variable can be computed from DNS or determined from experiments.

Lastly, Direct Numerical Simulations approach is the most powerful method to compute turbulent premixed flames. The DNS simulations have five levels [10]. At level zero each quantity is analyzed individually and instantaneously. At level one, each flame element is investigated along its normal direction. At level two the ensemble-averaged quantities are calculated throughout the flame in the flame normal direction. At level three, the spatially averaged quantities are determined. DNS allows computing local flame structures, such as strain, curvature, stretch, and flamelet structure. It also allows to compute complex chemistry simulations, creating a highly realistic simulation. The biggest problem to overcome is the expensive computation requirements of DNS [21].

The recent numerical studies of turbulent premixed Bunsen burners include algebraic flame surface density (FSD) modeling techniques. In order to evaluate their FSD model under high pressure conditions, Rasool et al. [22] performed direct numerical simulations. They found that the pressure increase has a detrimental effect on the predictions given by the FSD model, because of the decreasing flame thickness is requiring a much finer mesh and thus creates very high errors with FSD models. In a different study by Keil et al. [23], the authors used large eddy simulations on a bunsen burner to examine how elevated pressures affect the properties of FSD transport statistics. They found that modeling becomes noticeably more difficult when working with high pressures since the strain rate and curvature values are not predicted accurately. Numerical studies for premixed turbulent Bunsen burners have recently used algebraic flame surface wrinkling models (AFSW). Guerrero et al. [24] used the AFSW model to evaluate high pressure Bunsen burner experiments utilizing OpenFoam for up to 40% hydrogen addition to methane flames, and Kutkan et al. [25] compared the performance of OpenFoam with Ansys Fluent using the same ASFW model, and stated that XiFoam solver has a tendency to overpredict flame heights found by experiments compared to Ansys Fluent.

2.3 Experimental Techniques for Measuring Turbulent Premixed Flames

Laboratory measurements of turbulent premixed flames are based on a diversity of burner configurations, such as open unconfined flames like Bunsen-type burners or an oblique flame, which is essentially a flat flame; or confined flames such as a spherical flame.

The experimental data is useful for understanding flame properties such as flame structure and flame speed. The analysis of flame structure requires measurements of mean velocity, composition, and temperature, as well as the turbulent intensities of these fluctuations, their covariances, length scales, and probability density functions. These measurements can be performed using several optical and laser-based techniques.

In this chapter, we mainly focus on the optical experimental techniques we used in this thesis for characterizing turbulent premixed flames, namely on the chemiluminescence and laser-induced Mie scattering techniques. A detailed presentation of laser diagnostics employed in combustion applications are presented in Eckbreth's book [26].

The chemiluminescence method is commonly used for the flame front location identification as an optical non-intrusive experimental procedure. The technique is based on capturing flame emissions from unstable chemical species, using optical filters, for radicals, such as CH*, OH*, and C2*. Generally, CH* and OH* filters are used, as these emissions occur in the combustion zone and have very high intensities, therefore easy to capture in lean premixed combustion [27]. Also, under lean premixed conditions, C2* emission is not very significant compared to OH* and CH* [28]. It is important to note that, as the equivalence ratio decreases, both OH* and CH* radicals experience a decrease in light intensity for lean methane-air premixed flames [29, 30].

CH* and OH* species can be used as a marker for the heat release rate, as well as to identify the flame temperature and local equivalence ratio. There are different ideas

about which radical is a better indicator of the flame surface. Previous work concerning the turbulent flames with high strain concludes that the OH* radicals are not showing good agreement with the heat release, since OH* shows a variation with turbulence levels and may completely disappear at high strain rates [31].

Chemiluminescence has a variety of applications in the industry because of its very easy application methodology, but one should note that almost all applications of chemiluminescence mainly depend on the assumption of representing the heat release rate. Indeed, in parallel to its benefits, the chemiluminescence technique is a line-of-sight measurement technique and it is easily disturbed by other emissions in the flow field, which creates additional errors during data postprocessing. Souflas calculated the equivalence ratio field of a bluff-body stabilized, preheated propane-air flame using chemiluminescence measurements and discovered that maximum OH*/CH* ratio values represent the equivalence ratio trends while slightly under-estimating it due to the line-of-sight measurements [28]. Bedard et al. [31] used the chemiluminescence technique to detect combustor instabilities in a rocket combustor and refer to the downsides of the technique because of its dependence on pressure, strain rate, equivalence ratio, and turbulence level. The authors emphasize that it is very hard to decouple the CH* and OH* radicals from these flow field properties, and self-absorption of the radicals distorts the line-of-sight images.

Laser-induced Mie scattering technique can be used to determine the flame front location, by employing oil droplets or solid particles as flow seeding materials. The technique is based on the Mie theory which explains the elastic collisions between light scattering particles and an electromagnetic wavelength (which is the laser beam wavelength in combustion applications). Mie scattering and Rayleigh scattering techniques are based on this phenomenon [26]. The difference between them is that, for Rayleigh scattering the following restriction should be met:

$$\frac{2\pi d}{\lambda} \ll 1$$

where d represents the scattering particle diameter, λ is the laser wavelength. The equation means that the dimensions of scattering particles should be much smaller than the radiation wavelength, such as the flow species molecules. Mie scattering does not have this restriction, and it applies to particle diameters close to the wavelength of the light source.

Images of a premixed flame front can be captured by seeding the reactant stream with oil particles and illuminating it with a laser light sheet. As the droplets evaporate at the flame front, Mie scattering images are only collected from the unburnt side of the mixture allows to distinguish the unburnt – burnt gases frontier, that is the instantaneous flame front [32]. Mie scattering technique is used to collect tomographic images of instantaneous flame fronts from which the average flame front structure and the flame surface statistics can de deduced.

The two-dimensional nature of the laser-induced Mie scattering phenomena allows measurements of the flame front curvature. Curvature is defined as the inverse of the radius of the circle tangent to the curve at a specific point [33]. Flame elements convex to the fresh gas side correspond to a positive curvature, while a concave one means a negative curvature [4].

$$\kappa = \frac{d\psi}{ds} = \frac{1}{r} \tag{2.17}$$

where κ indicates curvature at point P, ψ is the slope angle of the tangent at P, s is the arclength and r is the radius of the circle tangent to the specific location P. A high degree of polynomial was fit into the flame front and divided into equal distances of ds. The division locations are used as the centers of the tangent circles.

Gülder et al. [34] used the Mie scattering images of a turbulent premixed propane-air flame to investigate the characteristics of the flame front surfaces. They demonstrated the near identicality of the fractal dimensions obtained from the OH-LIF and Mie scattering pictures, which they used to calculate the flame surface density, which is the flame surface area per unit volume, approximated as the flame length per unit surface area. Thiesset et al. [35] employed Mie scattering tomography

results to calculate the flame consumption speed. Very recently, Zheng et al. compared Mie scattering and OH-PLIF measurements for instantaneous flame front identification on a piloted premixed Bunsen flame for edge detection and proved that Mie scattering can be used to calculate the flame surface as well as OH-PLIF [36].

In order to comprehend the flow properties of turbulent flames, turbulent Bunsen burners are frequently utilized in experimental studies. The recent experimental work of turbulent premixed bunsen flames include the instability, three dimensional nature of the turbulent flame, and hydrogen addition effects. The first phenomenon studied is flame instabilities. For instance, Wang et al [37] investigated the effect of burner diameter on flames instabilities, while Toriani et al [38] conducted research on the self-wrinkling of flame fronts caused by Darrieus-Landau instabilities for turbulent premixed Bunsen flames. Zhang et al. [39] studied Darrieus-Landau instabilities to describe the relation between the integral length scale and the instability mode. The study of the properties of hydrogenated turbulent premixed flames is the second investigated phenomenon. Zhang et al. [40] used laser diagnostics to investigate the effect of hydrogen on the local flame structure and discovered that increased hydrogen conten promotes finer wrinkles in the flame. The effects of increased hydrogen addition to CH4/H2/air premixtures on the reduction of preheat thickness were shown in another work by Zhang et al. [41]. The three-dimensionality of the turbulent premixed flames is the subject of the third explored phenomenon in the literature . Zheng et al. [42] recently reported that the 3D characteristics were captured by Mie scattering measurements to evaluate the flame surface density values. To do this, they determined the 3D surface density of the flame by projecting the flame normal vector onto two measurement planes and calculated the direction angles on each plane. Additionally, Tyagi et al. [43] recently explored the three-dimensional structure of turbulent premixed Bunsen flames to statistically analyze three-dimensional flow propagation effects from two-dimensional experimental data. The effects of out-of-plane motion on flame propagation were assessed by the authors using theoretical and probabilistic models.

CHAPTER 3

METHODOLOGY

This chapter covers the experimental and numerical methodology used to investigate turbulent lean premixed flames. The exprimental setup elements and postprocessing methods are discussed. The numerical method, the solver used and the resolution schemes are discussed.

3.1 Experimental Methods

3.1.1 Experimental Setup Design

Experiments are completed on a newly designed and manufactured high pressure combustion chamber. The experimental apparatus includes a high pressure combustion chamber, a turbulent bunsen burner, a moving mechanism for the burner, and the gas line. The global layout of the experimental setup is given in Fig. 3.1.

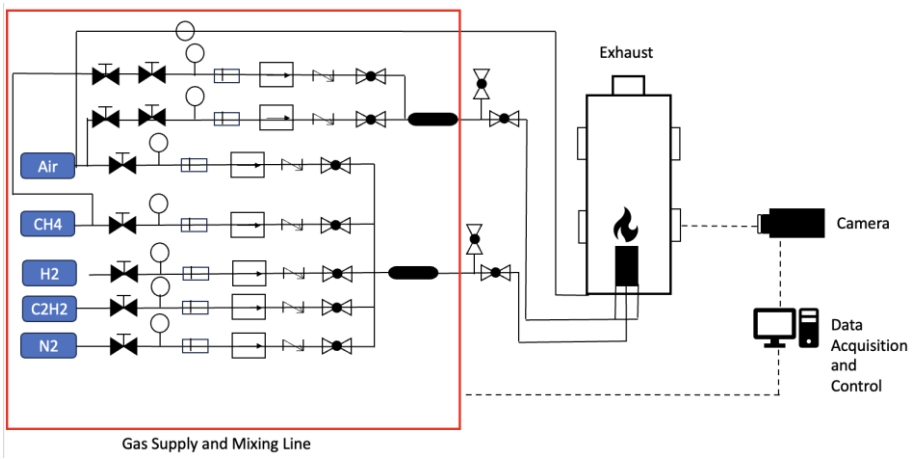

Figure 3.1. Schematic view of the experimental setup

3.1.1.1 High Pressure Chamber

The combustion chamber is made up of two separate parts, equiped by three windows mounted for optical measurements of the turbulent Bunsen flame. The stainless-steel modules, 600 mm in height and 300 mm in diameter are identical and they are cooled by water pipes to prevent condensation inside the chamber. The chamber operates between pressures of 0.1 and 0.9 MPa .

The bottom module of the combustion chamber is mounted on a square AISI304 plate of 600 mm and 40 mm thickness. The bottom module is closed with a blind flange which is connected with bolts to the module. Inside the blind flange, there exists a part to connect the Bunsen burner, which allows the burner to move axially and ensures impermeability. All the connections to pressurize the burner and water drainage are mounted on the blind flange.

At the bottom module, a Bunsen burner with a perforated plate as a turbulence generator is placed. The perforated plate is interchangeable to enable the investigation of various turbulence structures and produces uniform turbulence. The chamber allows optical measurements and has thermocouples and pressure transducers installed for controlling the inside environment. In the bottom chamber module, three quartz windows allow optical measurements of the flame from various angles.

The high-pressure burner facility can be used with various compatible burners which may be installed on the blind flange at the bottom of the lower module.

The top and bottom modules of the combustion chamber are identical. The modules are manufactured as double-walled with AISI 304 stainless steel. The double-walled system allows the water cooling system of the combustion chamber. The cooling water enters from the bottom side of both modules and exits from the top side. For each of the modules, 6.5 l/min cooling water is required.

Both modules have 4 window openings. Only the bottom module has 3 glass windows, and all other windows are closed with metal disks. The quartz windows allow for optical measurements of the flame, the glasses are temperature and pressure resistant. The metal disk on the bottom module is used for connecting the ignition electrode, while the metal disks on the top module are used for connecting a thermocouple and a pressure transducer.

At the topmost part of the combustion chamber, there exists a heat exchanger and a cap for exhaust. The exhaust gases are condensed as tap water with a 6.5 l/min flow rate passes through the heat exchanger. The heat capacity is 10 kW and the dimensions of the heat exchanger are Ø 10 mmx1mm TP316 pipes. The cap is used for connecting the exhaust and safety parts of the module. In this part, there is a back pressure regulating valve to adjust the inside pressure of the combustion chamber, two proportional control valves, and a rupture disk for safety measures.

3.1.1.2 The Burner

The turbulent Bunsen burner is made up of three parts placed inside each other. The two innermost pieces are brass of and the outer cylinder is made of AISI304 stainless steel. The innermost port is used for the main mixture feeding, the second port is for the pilot flame. The third outlet port is for another gas flow to shield the flame from its surroundings but is not used in the scope of this thesis. The diameter of the main premixture burner outlet is 25 mm, and the height of the burner is 230 mm. To generate homogeneous turbulence, a perforated plate is installed 50 mm upstream of the burner exit. The perforated plate is made of titanium, 1 mm thick, and has 2.5 mm diameter holes with a 3.5 mm pitch. The perforated plate is interchangeable so that the system allows for measurements at various turbulence parameters, such as the tubulence intensity and length scales. The perforated plate used in the present experiments has a blockage ratio of 42%.

The main flame is ignited with the help of a continuous pilot flame, which surrounds the main burner outlet with an annular width of 2.5 mm. The pilot flame is a stoichiometric methane-air mixture for each test case, and the flow rate supplied to the pilot flame is always 13% of the total premixture flow rate in the main inlet. The pilot flame is controlled with another gas line, having two mass flow controllers for air and methane, and has a separate inline static mixer. The pilot flame is always on during the experiments.

The ignition is provided with a tungsten igniter. The igniter is a standard boiler igniter, has a 1 kV ignition transformer box, and is connected to the PLC system. The electric ignition is adjusted using the control unit. The ignition part is connected to the metal disk on the bottom module and a swedge lock ensures the impermeability of that part.

The Burner power is 1.7 kW at 0.1 MPa during the atmospheric experiments conducted throughout this study.

Figure 3.2. Technical drawings of the burner, showing the interior design

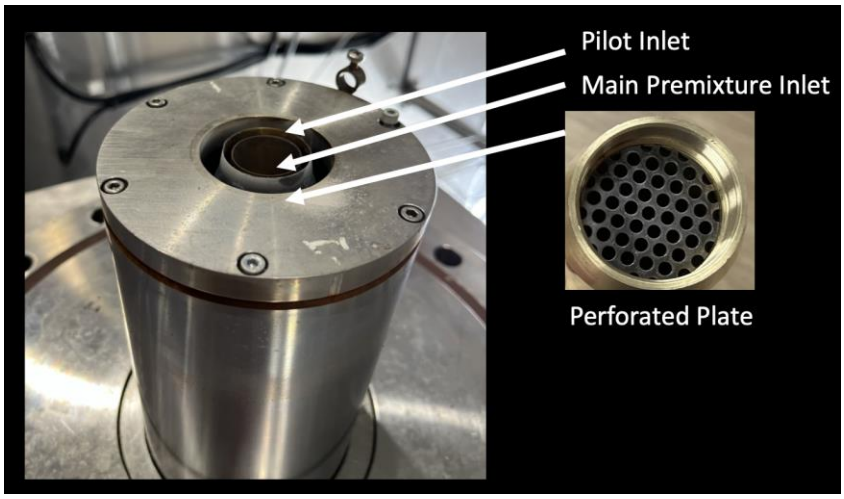

Figure 3.3. The Bunsen burner and the perforated plate as the turbulence generator

3.1.1.3 Burner Displacement Mechanism

The burner can move axially with the help of a stepper motor. Also, two pistons working under the chamber pressure support the system from the bottom.

The movement is performed by using a direct drive servo motor of power 3kW, 20Nm. The servo motor has a 1/10 gear reducer mounted. The movement of the burner is transmitted with a single-threaded shaft, which has a 5 mm pitch and 40 mm diameter. Two guide shafts are used to prevent unwanted motions. The guide shafts are mounted inside the moving plates on two sides, where there are two linear bearings. There are two pneumatic pistons to balance the pressurization force inside the chamber.

The combustion chamber, the moving platform, and the burner are mounted on a platform of 600mm x 600 mm dimensions. The platform is manufactured from a 50x50x4 square profile.

3.1.1.4 Gas Distribution and Mixing System

The Bunsen burner presented in this study works with premixed fuels, therefore the gas mixing line is designed accordingly. In the gas supply system, there are two separate parts. The first part is for the main flame premixture and the second part is for the pilot flame premixture. The main premixture part consists of five separate gas lines, in each gas line three mass flow controllers control the gas inlet flow rates of air, CH_4, and H_2. Through the line, the gas pressure is monitored continuously with pressure transducers on each gas line. The main line has 5 branches for air, CH_4, H_2, C_2H_4 (not used in this work), and N_2.

All three air, methane, and hydrogen lines have a needle valve (ball valve in the air line), pressure sensor, filter, mass flow controller (MFC), check valve, and ball valve, respectively.

There are check valves and ball valves in the nitrogen line. In addition to the connection of the nitrogen line to the fuel mixture, purging is also provided by T-joints from the N_2 line. The purge line is connected to all fuel lines after a check valve and ball valve. At the end of the mainline, all fuel inlets are connected to the mainline static mixer.

The pilot line consists of 2 branches which are the air and CH_4 line. The pilot line is a ¼" pipe. Both branches have a needle valve, pressure sensor, filter, MFC, check valve, and ball valve. The pilot methane line is separated from the main methane line with the help of a ball valve and connected to the pilot line. The exits of the two branches are connected to the pilot line static mixer.

Both gas mixers are homemade from a stainless-steel pipe of 1-inch diameter and 25-inch length filled with glass beads. The static inline mixer for the main line has 5 inlets to allow mixtures of air, CH_4, H_2, C_2H_4 and N_2; while the inline static mixer for the pilot line has two inlets for air and CH_4.

The static mixer is shown in Fig. 3.4.

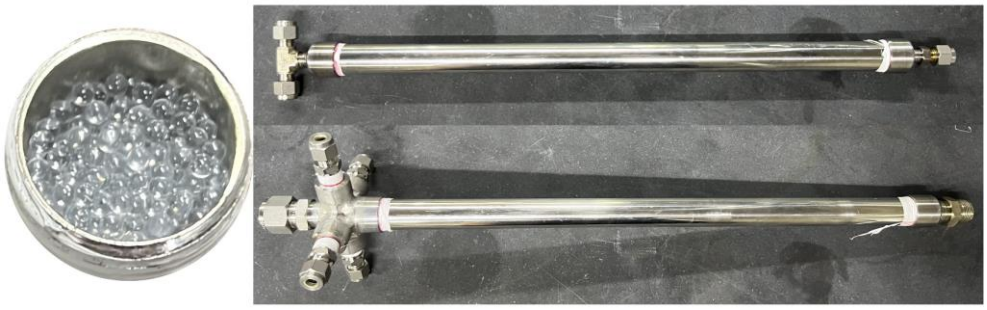

Figure 3.4. Static mixers and the glass beads

3.1.1.5 Operating Conditions and Experimental Matrix

A typical image of the investigated flames is shown in Fig. 3.5. The Bunsen burner was shown in Fig. 3.3 The burner allows the stabilization of turbulent flames for various fuel mixtures. The pilot flame helps for the stabilization of lean premixed flames.

Figure 3.5. The turbulent premixed flame with 0.8 equivalence ratio with no hydrogen addition

In the experiments, flames with equivalence ratios of 0.6, 0.7, and 0.8 are investigated, for molar hydrogen addition rates of 0%, 10%, and 20% to the main

fuel which is natural gas in this study. The Reynolds number is kept constant in all experiments, by fixing the inlet premixture velocity at 1.90 m/s.

The experimental matrix with the flow rates is presented in Table 3.1, where CL is for the chemiluminescence measurements, MIE denotes Mie scattering measurements and XI means that numerical simulations are performed for the corresponding condition.

Table 3.1. Experimental Matrix

H_2 [mol%]	0	10	20
$\phi = 0.6$	CL, MIE, XI	CL, MIE, XI	CL, MIE, XI
$\phi = 0.7$	CL, MIE, XI	CL, MIE, XI	CL, MIE, XI
$\phi = 0.8$	CL, MIE, XI	CL, MIE, XI	CL, MIE, XI

3.1.2 Chemiluminescence Measurements

Being a non-intrusive optical technique, which does not require the usage of a laser, chemiluminescence measurements are easily applied as a simple optical measurement technique for combustion applications. In the present study, chemiluminescence emissions serve as a measure of the heat release rate. The heat release rate is then utilized as an indicator of the progress variable c. For turbulent flames, some studies show that the OH* chemiluminescence is a weaker marker for the heat release rate, and both OH* and CH* radicals should be used as the heat release rate marker [31, 44-45]. In this study images from both radicals are collected using the same camera angle and the hydrogen addition effect is investigated using the OH* and CH* radicals chemiluminescence intensities. Hydrogen, by changing the Lewis number of the mixture, is expected to have a strong effect on the chemiluminescence intensity [27]

The chemiluminescence results can also be used to calculate the laminar and turbulent flame speeds [46-47]. In this study, it is used to investigate the turbulent flame speed and the flame height under various conditions.

Chemiluminescence images are captured using the optical set-up and the intensified Dantec HiSense Zyla camera available at TÜBİTAK-SAGE. The line-of-sight images are collected using two filters, an OH* filter with a bandpass of 300-325 nm and a CH* filter with a bandpass of 420-440 nm. The camera exposure time is set to 250 µs, while the intensifier gain is 50. In each experiment, 1000 images are collected within 1s. Therefore, the images are collected at 1 ms time intervals. Image processing is performed using MATLAB.

Flame height and the turbulent flame speed are calculated using the chemiluminescence images. The effect of hydrogen addition and equivalence ratio changes are then investigated.

Figure 3.6. The chemiluminescence measurement system

3.1.3 Laser Induced Mie Scattering Measurements

Mie scattering technique using liquid droplets is a way to determine the flame edge location, since the droplets evaporate at the flame front allowing to distinguish the cold unburnt and hot burnt gases separated by the instantaneous flame front [36], as defined in Chapter 2.

Mie scattering experiments are performed using a continuous, 532 nm solid-state laser of 4 W power also available at TÜBİTAK-SAGE. The premixture is seeded by olive oil droplets using an olive oil injector in the premixture line, just before the burner entrance. The 2D images are collected at 240 fps using a 532nm bandpass filter, with 3840x2160 pixels. 500 frames are used for investigating each case. A MATLAB code is developed and used to postprocess the results, which are explained in the Results chapter. The Mie scattering results are employed to investigate the flame front geometry and curvatures, the flame height, the flame brush thickness and the turbulent flame speed. The equivalence ratio and hydrogen addition effects are investigated and compared with the chemiluminescence measurements.

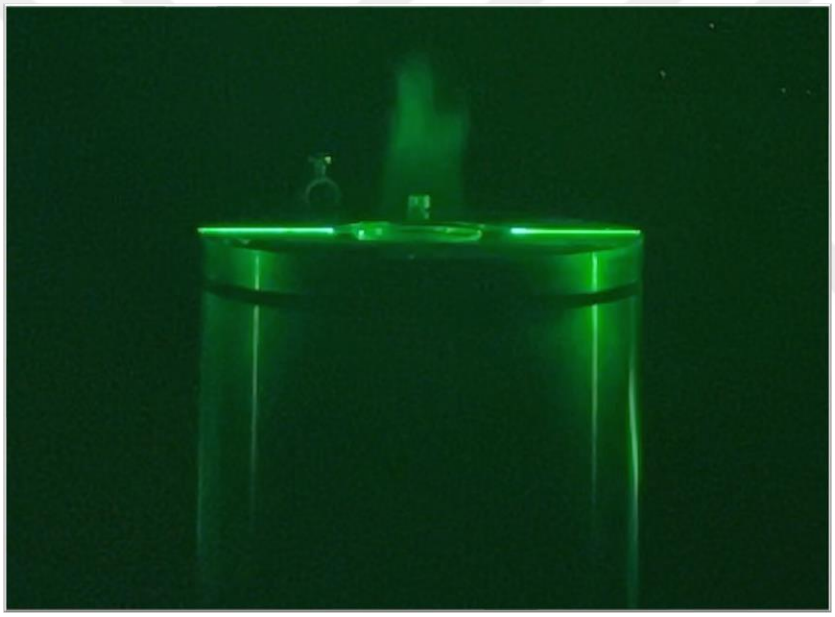

Figure 3.7. Raw Mie Scattering image, in which the flame is seeded by olive oil droplets

3.2 Numerical Methods

3.2.1 Governing Equations

The general equations of continuity, momentum and enthalpy are as follows [10]:

$$\frac{\partial \rho}{\partial t} + \frac{\partial \rho u_i}{\partial x_i} = 0 \tag{3.1}$$

$$\frac{\partial}{\partial t}\rho u_j + \frac{\partial}{\partial x_i}\rho u_i u_j = -\frac{\partial p}{\partial x_j} + \frac{\partial \tau_{ij}}{\partial x_i} + \rho \sum_{k=1}^{N} Y_k f_{k,j} \tag{3.2}$$

$$\rho \frac{Dh_s}{Dt} = \dot{\omega}_T + \frac{Dp}{Dt} + \frac{\partial}{\partial x_i}\left(\lambda \frac{\partial T}{\partial x_i}\right) - \frac{\partial}{\partial x_i}\left(\rho \sum_{k=1}^{N} h_{s,k} Y_k V_{k,i}\right) + \tau_{ij}\frac{\partial u_i}{\partial x_j} + \dot{Q} + \rho \sum_{k=1}^{N} Y_k f_{k,i} V_{k,i} \tag{3.3}$$

In the momentum equation, the volume force, or $f_{k,j}$, is acting in direction j on species k. The energy equation is in the sensible enthalpy form. Therefore, the following equations are necessary to define the whole equation set:

$$h_s = h - \sum_{k=1}^{N} \Delta h_{f,k}^{\circ} Y_k \tag{3.4}$$

where h denotes enthalpy, q is the heat flux, $\dot{Q}$ is heat source term, and $\dot{\omega}_T$ is the heat produced by combustion. The species equation is not presented since the solver used in the scope of the thesis does not deal with species conservation.

The first equation describes the conservation of mass; the second equation governs the conservation of momentum; and the third equation deals with the conservation of energy. In the case of laminar and viscous flows, solving the N-S Equations are sufficient. However, for turbulent flows, the turbulence scales must be modeled or numerically resolved. There are three methods to describe turbulent flows as addressed in the literature review part of the thesis, which are RANS, LES and DNS. RANS and LES methods are employed in this thesis. RANS is only used to check the quality of LES, and LES is utilized to model the reacting flow. Therefore, RANS equations are only shortly described in this chapter, and LES equations are more deeply detailed.

RANS method consists of modifying the N-S equations in a form that calculates the mean and fluctuating components of the velocity through Reynolds decomposition, which separates the velocity into mean and fluctuating components. The RANS

equations include extra stress terms introduced by the turbulent fluctuations, and the equations model turbulence effects in a time averaged form.

The numerical mesh quality evaluation is completed by conducting a RANS modeling with standard $k-\varepsilon$ turbulence model. The $k-\varepsilon$ formulation in Openfoam, together with the N-S equations, are as follows:

$$\mu_T = C_\mu \rho \frac{k^2}{\varepsilon} \tag{3.5}$$

Here, ε is the total dissipartion rate, μ_T and k are the eddy viscosity and kinetic energy of the turbulent fluctuations. The solved k- ε equations are as follows:

$$\rho \frac{\partial k}{\partial t} + \rho \langle u_j \rangle \frac{\partial k}{\partial x_j} = 2\,\mu_T \langle S_{ij} \rangle \frac{\partial \langle u_i \rangle}{\partial x_j} - \rho\varepsilon + \frac{\partial}{\partial x_j} + \left[\left(\mu + \frac{\mu_T}{\sigma_k} \right) \frac{\partial k}{\partial x_j} \right] \tag{3.6}$$

$$\rho \frac{\partial \varepsilon}{\partial t} + \rho \langle u_j \rangle \frac{\partial \varepsilon}{\partial x_j} = C_{\varepsilon 1} P_k \frac{\varepsilon^2}{k} - C_{\varepsilon 2} \rho \frac{\varepsilon^2}{k} + \frac{\partial}{\partial x_j} \left[\left(\mu + \frac{\mu_T}{\sigma_\varepsilon} \right) \frac{\partial \varepsilon}{\partial x_j} \right] \tag{3.9}$$

The standard constants in the solver are $C_\mu = 0.09$, $C_{\varepsilon 1} = 1.44$, $C_{\varepsilon 2} = 1.92$, $\sigma_k = 1.0$ and $\sigma_\varepsilon = 1.3$.

The computations in this thesis are mainly conducted using Large Eddy Simulations (LES). As mentioned in Chapter 2, large eddy simulations solve the instantaneous flow equations. The larger eddies are geometry and flow dependent while sub-grid scale turbulent diffusion depends on flow variables. The three-dimensional turbulent motion represented by geometry dependent, anisotropic, and 3-D eddies which contain most of the turbulent energy is explicitly solved, while the smaller scale motions which have a universal behavior are modeled.

LES is necessary for resolving flow problems with intrinsic unsteady features, such as bluff-body, external aerodynamics, and channel flows. In terms of computational expense, it lies between RANS and DNS. The filtering operation is defined below, where F corresponds to the LES filter and f is the filtered quantity, as:

$$\bar{f}(\mathrm{x}) = \int f(x')F(x - x')dx' \tag{3.10}$$

The velocity and pressure are represented through a filtering operation as follows:

$$u_i = \bar{u}_i + u_i' \tag{3.11}$$
$$P_i = \bar{P}_i + P_i'$$

For compressible flows, the density is not constant. Therefore, the Favre filtering is employed [48]:

$$\tilde{f} = \frac{\overline{\rho f}}{\bar{\rho}} \tag{3.12}$$

$$\bar{\rho}\tilde{f}(\mathrm{x}) = \int \rho f(x')F(x - x')dx' \tag{3.13}$$

The properties of Favre filtering are:

$$f' = f - \bar{f} \tag{3.14}$$
$$f = \tilde{f} + f'' \tag{3.15}$$
$$f'' \neq 0 \tag{3.16}$$
$$\tilde{\tilde{f}} \neq \tilde{f} \tag{3.17}$$

Using the Favre filtering, the f' values define the subgrid scale values of the flow, which are unresolved in LES. For reacting flows, the LES equations are the filtered versions of equations (3.3) to (3.5).

The continuity equation (conservation of mass) is:

$$\frac{\partial \bar{\rho}}{\partial t} + \frac{\partial}{\partial x_i}(\bar{\rho}\tilde{u}_i) = 0 \tag{3.18}$$

The momentum equation writes:

$$\frac{\partial \bar{\rho}\tilde{u}_i}{\partial t} + \frac{\partial}{\partial x_i}\left(\bar{\rho}\tilde{u}_i\tilde{u}_j\right) + \frac{\partial \bar{p}}{\partial x_j} = \frac{\partial}{\partial x_i}[\bar{\tau}_{\mathrm{ij}} - \bar{\rho}(\widetilde{u_i u_j} - \tilde{u}_i\tilde{u}_{\mathrm{j}})] \tag{3.19}$$

where τ_{ij} is the residual stress tensor. Using the residual stress tensor, the residual kinetic energy is calculated as:

$$\mathrm{k_r} = \frac{1}{2}\tau_{ij} \tag{3.20}$$

The anisotropic residual stress tensor, which represents the physical relation between modelled and unmodelled scales is:

$$\tau_{\mathrm{ij}}^{r} = \tau_{ij} - \frac{2}{3}k_r\delta_{ij} \tag{3.21}$$

Here, $\frac{2}{3}k_r\delta_{ij}$ is named as the isotropic residual stress. It can also be incorporated into a modified pressure:

$$\tilde{P} = \widetilde{P_F} + \frac{2}{3}k_r \tag{3.22}$$

τ_{ij}^{r} is the Sub Grid Scale (SGS) tensor and it needs to be modelled. It is modelled using the eddy viscosity approximation [45], to simulate the behavior of k in OpenFoam.

$$\tau_{ij} \approx \frac{2}{3}k_{sgs}\delta_{ij} - 2\nu_{sgs}\, dev(\bar{D})_{ij} \tag{3.23}$$

$$\bar{D}_{ij} = \frac{1}{2}\left(\frac{\partial \bar{u}_i}{\partial x_j} + \frac{\partial \bar{u}_j}{\partial x_i}\right) \tag{3.24}$$

$$k_{sgs} = \frac{1}{2}\,\tau_{kk} = \frac{1}{2}\,(\overline{u_k u_k} - \overline{u_k}\,\overline{u_k}) \tag{3.25}$$

$$\nu_{sgs} = C_k\sqrt{k_{sgs}}\,\Delta \tag{3.26}$$

Finally, the energy equation in the enthalpy form is written as:

$$\frac{\partial \bar{\rho}\tilde{h}_s}{\partial t} + \frac{\partial}{\partial x_i}\left(\bar{\rho} u_i \tilde{h}_s\right) = \frac{\partial \bar{p}}{\partial t} + \overline{u_\iota \frac{\partial p}{\partial x_\iota}} + \frac{\partial}{\partial x_i}\left[\overline{\lambda \frac{\partial T}{\partial x_\iota}} - \bar{\rho}\left(\widetilde{u_\iota h_s} - \tilde{u}_i \tilde{h}_s\right)\right] + \overline{\tau_{\iota J} \frac{\partial u_\iota}{\partial x_J}} - \frac{\partial}{\partial x_i}\left(\overline{\rho \sum_{k=1}^{N} V_{k,\iota} Y_k h_{s,k}}\right) + \bar{\dot{\omega}}_T \tag{3.27}$$

where $\left(\widetilde{u_\iota h_s} - \tilde{u}_i \tilde{h}_s\right)$ denotes unresolved enthalpy flux and $\tau_{ij} = \widetilde{u_i u_j} - \tilde{u}_i \tilde{u}_j$ denotes the unresolved Reynolds stresses.

The thesis deals with reacting LES computations using One-Equation Eddy Viscosity Model (k-Equation in OpenFoam). This model calculates k_{sgs} with a transport equation, therefore k_{sgs} is not constant in the domain. The turbulent kinetic energy in k-equation (One-Equation Eddy Viscosity Model) in OpenFoam is calculated as:

$$\frac{D}{Dt}(\rho k) = \nabla \cdot (\rho D_k \nabla k) + \rho G - \frac{2}{3}\rho k \nabla \cdot \boldsymbol{u} - \frac{C_e \rho k^{1.5}}{\Delta} + S_k \tag{3.28}$$

where $C_e = 1.408$ and $C_k = 0.094$ by default.

The ideal gas law is used during the simulations.

$$P = \rho R T \tag{3.29}$$

3.2.2 Geometry and Meshing of the Numerical Setup

Only the bottom module of the chamber is modelled up to 12D height, which is 300 mm, to shorten the computation time in the numerical simulations. The perforated plate and the burner are modeled as they are geometrically.

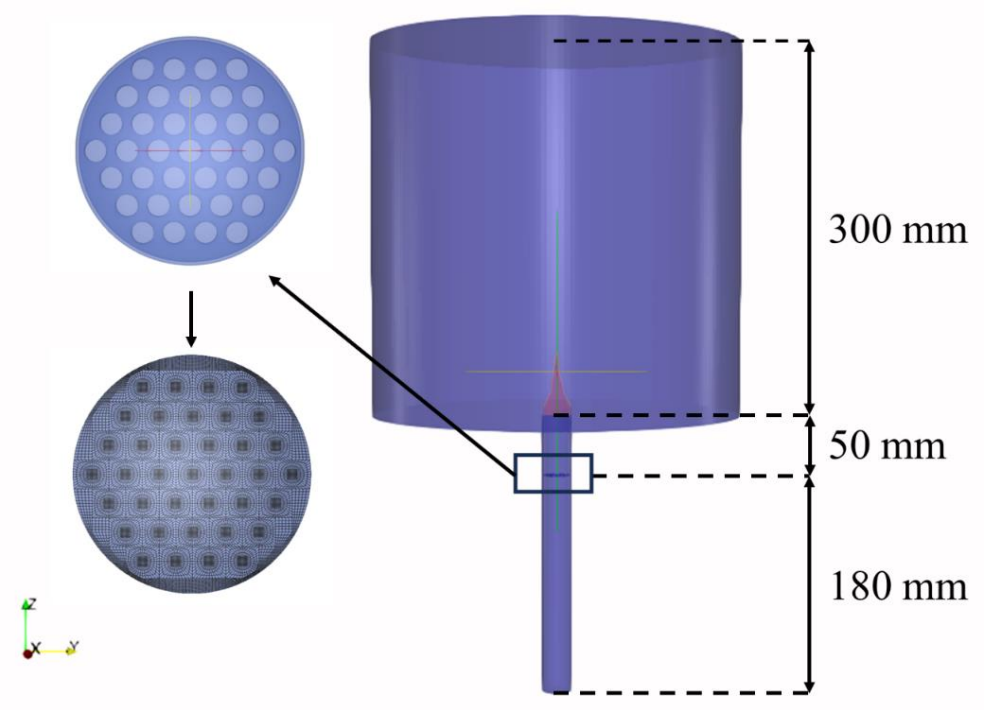

Figure 3.8. The schematic of the computational domain

Before constructing the numerical mesh system, the required resolution to ensure y+ values of one or less is computed as 1.23e-4 m by using a self-similar Blasius boundary layer solution. the flame thickness is then calculated to provide insight for the mesh dimensions in the possible flame areas. The laminar flame thickness is calculated using the following formulation [10].

$$\delta_L = \frac{T_b - T_u}{\max\left(\frac{dT}{dx}\right)} \tag{3.30}$$

For calculating the laminar flame thickness, a one dimensional free flame is modeled with Cantera [49] for each hydrogen addition rate and equivalence ratio. The laminar flame thickness values are summarized in Table 3.2.

Table 3.2. Laminar flame thickness values for the experimental matrix [mm]

H_2 [mol%]	0	10	20
$\phi = 0.6$	0.975	0.924	0.866
$\phi = 0.7$	0.666	0.637	0.605
$\phi = 0.8$	0.534	0.513	0.490

When constructing the mesh, these thicknesses are taken into account. The laminar flame thickness with changing equivalence ratio and hydrogen addition rates are shown in Fig. 3.9.

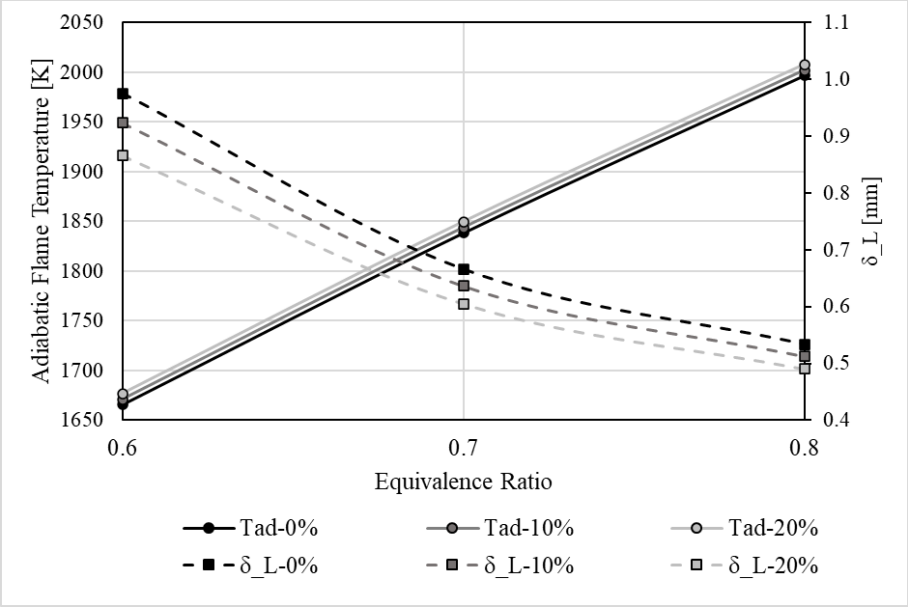

Figure 3.9. Adiabatic Flame Temperature and Laminar Flame Thickness for Different Hydrogen Addition Rates vs Equivalence Ratio

Regarding the y+ and laminar flame thickness calculations for the mesh constrictions, two different hexahedral meshes are constructed for the cold simulations, consisting of 5.5 million and 9.3 million cells, respectively . The mesh is specifically refined in the perforated plate area, wall regions, and the expected flame region according to the mentioned mesh criterion. Reynolds Averaged Navier Stokes Simulations are performed for the cold flow simulations using the RANS $k - \varepsilon$ turbulence model. This simulation is used as the first investigation of the mesh

size to lead better LES qualifications. A method to control the Pope criterion of solving more than 80% of the kinetic energy is the first check if integral length scale is resolved enough [50]. In the scope of this thesis, a variable named f is defined, which is the number of meshes that fits inside the integral length scale. It is assumed that if the mesh is resolved enough, it should be fitting at least 5 cells in the integral length scale in more than 80% of the domain (Eqs. 3.26 and 3.27). Fig 3.10 shows the f criterion, which proves that more than 5 cells fit into the integral length scale at almost all parts of the domain, meeting the Pope criteria in the RANS simulations.

Lastly, the mesh is controlled by a non-reacting flow LES simulation.

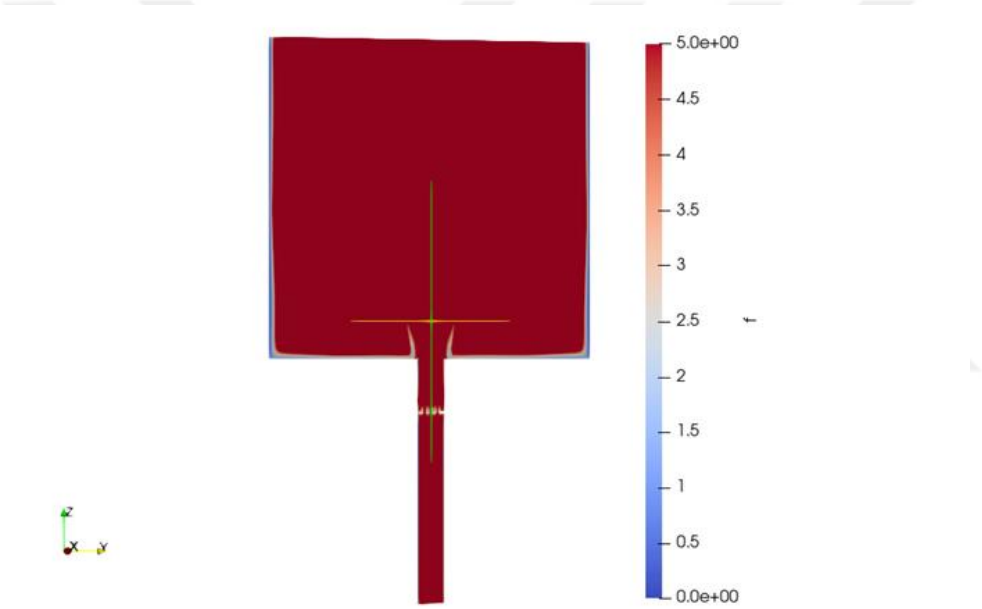

Figure 3.10. The field of mesh criterion f for the coarse mesh

$$I_0 = \frac{k^{3/2}}{\varepsilon} \tag{3.31}$$

$$f = \frac{I_0}{\sqrt[3]{Cell\ Volume}} < 5 \tag{3.32}$$

Figure 3.10 shows that the f field for the 5.5 million mesh meets the 80% criterion, by having cells that are smaller than one-fifth of the integral length scale in almost all the domain.

Finally, the LES mesh is checked to resolve 80% of k in the domain with the local mesh [50] instantaneously. For this, air is selected as the working fluid in the domain for non-reacting LES simulations with pisoFoam solver. The turbulent kinetic energy is calculated as:

$$k = \frac{1}{2}\left(\overline{(u')^2} + \overline{(v')^2} + \overline{(w')^2}\right) \tag{3.33}$$

In order to check this, a variable named as RATIO is defined, which is:

$$RATIO = \frac{k_{res}}{k_{res} + k_{sgs}} \tag{3.34}$$

The RATIO variable should be less than 0.8 in most parts of the domain to ensure that more than 80% of the kinetic energy is resolved instantaneously. The contours of RATIO are shown in Figs. 3.11.

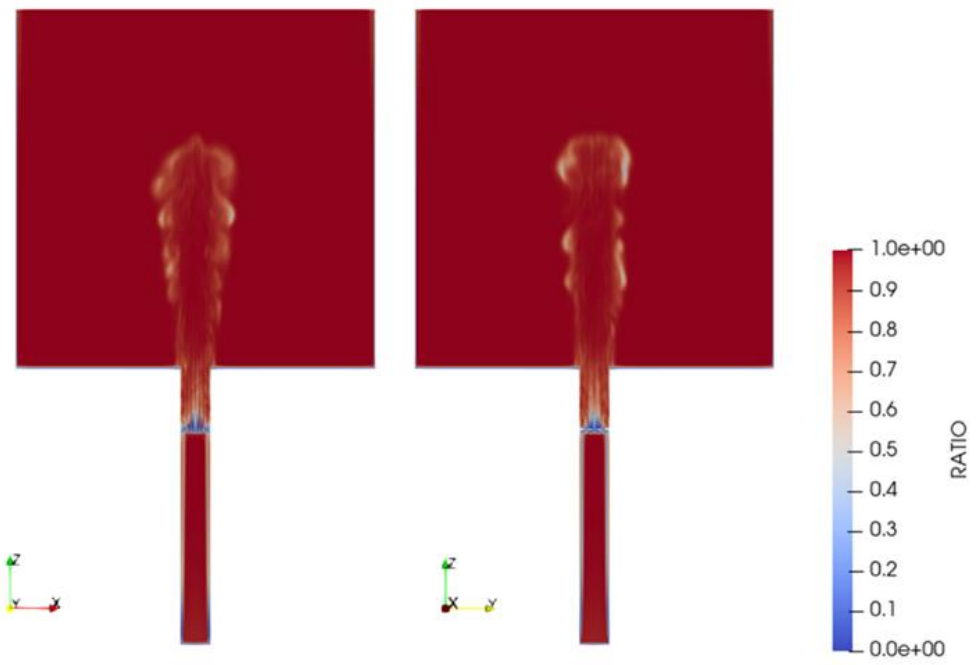

Figure 3.11. Turbulent kinetic energy ratios (RATIO) resolved in the domain in xz and yz planes.

3.2.3 The XiFoam Solver

In this work, the XiFoam solver of OpenFoam1912 [51] is used to model the reactive turbulent flow. The premixed combustion solver is based on the Weller $b - \Xi$ flame surface wrinkling combustion model [52].

The computations with XiFoam solver are performed for a conservative formulation of the mass, momentum, and enthalpy equations using large eddy simulations. A variable specific heat is calculated using the JANAF tables in polynomial form, which will be explained later. The dynamic viscosity is based on the Sutherland law. Turbulence modeling is achieved using a one-equation (k model). The solved LES equations are given below.

To model the combustion process, the XiFoam solver integrates the transport equation for the so-called regression variable b, weighted by the density to maintain the conservative solution. The combustion process is calculated by creating a transport equation set with the laminar flamelet approach with conditional filtering.

The continuity equation is conditioned on the reactants side before filtering. To calculate the transport equation of the resolved part of the regression variable b is calculated instead of solving the progress variable c.

$$b = 1 - c \tag{3.35}$$

$$b = 1 - \frac{T - T_u}{T_b - T_u} \tag{3.36}$$

$$\frac{\partial\, \bar{\rho}\, \tilde{b}}{\partial t} + \nabla_s \left(\bar{\rho}\, \widetilde{U_u}\, \tilde{b}\right) = -\rho_u S_u \Xi \left|\Delta \bar{b}\right| \tag{3.37}$$

$$\bar{p_u}\ \bar{b} = \bar{\rho}\tilde{b} \tag{3.38}$$

The overbar symbols – and ~ represent the filtering and density-weighted Favre filtering operations [48] while the subscripts u and b represent conditioning on the unburned and burnt gases, respectively. Subgrid flame wrinkling factor Ξ is related to the flame surface area density Σ by:

$$\Sigma = \Xi \left|\Delta \bar{b}\right| \tag{3.39}$$

The conditionally filtered unburned gas velocity is modelled as:

$$\widetilde{\boldsymbol{U}}_{\boldsymbol{u}} = \widetilde{\boldsymbol{U}} + \left(1 - \tilde{b}\right)\overline{\boldsymbol{U}}_{\boldsymbol{ub}} \tag{3.40}$$

In LES form the algebraic model for $\overline{\boldsymbol{U}}_{\boldsymbol{ub}}$ with the countergrdient modelling is:

$$\overline{\boldsymbol{U}}_{\boldsymbol{ub}} = \left(\frac{\bar{\rho}_u}{\bar{\rho}_b} - 1\right) S_u \, \Xi \, \hat{\boldsymbol{n}} - \mathcal{D} \frac{\nabla \tilde{b}}{\tilde{b}\,(1 - \tilde{b})} \tag{3.41}$$

$$\hat{\boldsymbol{n}} = \nabla \tilde{b} \,/ |\nabla \, b| \tag{3.42}$$

Here, $\bar{\rho}_u$ / $\bar{\rho}_b$represents the density ratio of unburned and burned states, $\mathcal{D}$ represents the subgrid diffusion coefficient, S_u is the laminar flame speed and $\hat{\boldsymbol{n}}$ is the resolved flame normal.

The transport equation of b is therefore:

$$\frac{\partial \bar{\rho} \tilde{b}}{\partial t} + \nabla \cdot \left(\bar{\rho} \widetilde{\boldsymbol{U}} \tilde{b}\right) - \nabla \cdot \left(\bar{\rho}\, \mathcal{D}\, \nabla \tilde{b}\right) = -\bar{\rho}_u \, S_u \, \Xi \left|\nabla \, \tilde{b}\right| \tag{3.43}$$

The transport equations are used for the subgrid flame area density and the resolved regress variable b; the transport equations for the subgrid flame wrinkling Ξ can be written as:

$$\frac{\partial \, \Xi}{\partial t} + \widetilde{\boldsymbol{U}} \cdot \nabla \, \Xi = -\widetilde{\boldsymbol{n} \cdot (\nabla \boldsymbol{U}_s) \cdot \boldsymbol{n}} \, \Xi + \hat{\boldsymbol{n}} \cdot \left(\nabla \widetilde{\boldsymbol{U}_t}\right) \cdot \hat{\boldsymbol{n}} \Xi + \left(\widetilde{\boldsymbol{U}_t} - \widetilde{\boldsymbol{U}_s}\right) \cdot \frac{\nabla \left|\nabla \bar{b}\right|}{\left|\nabla \bar{b}\right|} \, \Xi \tag{3.44}$$

$$\partial \bar{b} / \partial t + \widetilde{\boldsymbol{U}_t} \nabla \bar{b} = 0 \tag{3.45}$$

In these equations, $\widetilde{\boldsymbol{U}_t}$ is the surface-filtered effective velocity of the flame and $\boldsymbol{U}_s$ is the local instantaneous velocity of the flame surface.

The strain effect on Ξ is represented by $-\widehat{\boldsymbol{n}\cdot(\nabla\widehat{\boldsymbol{U}_s})\cdot\boldsymbol{n}}\,\Xi$, and propagation of Ξ is shown by the second term $\widehat{\boldsymbol{n}}\cdot\left(\nabla\widehat{\boldsymbol{U}_t}\right)\cdot\widehat{\boldsymbol{n}}\Xi$ in the equation. They are both resolved in the subgrid, and modeled by decomposing them into resolved strain rates, σ_t and σ_s, and the subgrid turbulent generation/removal rates of G Ξ and R (Ξ -1). The strain rates are featured as $\widehat{\boldsymbol{U}_t}$ and $\widehat{\boldsymbol{U}_s}$, respectively, and G and R must be modeled. The distribution of Ξ through the flame is affected by differential propagation in a way that increases generation in the back of the flame and decreases generation up front, as shown by the third term on the right-hand side of the equation. By directly incorporating the effect into the model for G, the term's high-order derivatives, which provide computational challenges for LES, are avoided, leading to the simplified equation for Ξ:

$$\frac{\partial\,\Xi}{\partial t}+\widehat{\boldsymbol{U}_s}\cdot\nabla\Xi=G\,\Xi-R(\Xi-1)+(\sigma_s-\sigma_t)\Xi \tag{3.46}$$

XiFoam solver employs a spectral approach to model the turbulence-flame interaction. Here, the flame wrinkling is decomposed into a spectrum of length scales. The subgrid flame properties can be derived using this method by integrating over the relevant region of the spectrum. The model in XiFoam employs Gülder's turbulent flame speed correlation of [53]:

$$\frac{S_T}{S_L}-1=0.62\left(\frac{u'}{S_L}\right)^{0.5}R_\eta \tag{3.47}$$

where the turbulent flame speed is S_T, laminar flame speed is S_L, and the Kolmogorov Reynolds number R_η is equal to $R_\eta\approx Re_L^{1/4}$. The 0.62 coefficient is based on Gülder's experimental data. In the b-Xi equation set, the variable $\frac{S_T}{S_L}$ in Gülder's turbulent flame speed correlation is referred to as Ξ_{eq}^{*}, which is the algebraic expression of the flame wrinkling factor Ξ, as follows:

$$G = R\frac{\Xi_{eq} - 1}{\Xi_{eq} - 1} \tag{3.48}$$

$$R = \frac{0.28}{\tau_\eta}\frac{\Xi^*_{eq}}{\Xi^*_{eq} - 1} \tag{3.49}$$

$$\Xi^*_{eq} = 1 + 0.62\sqrt{\frac{u'}{S_u}}\mathcal{R}_\eta \tag{3.50}$$

$$\Xi_{eq} = 1 + 2(1 - b)(\Xi^*_{eq} - 1) \tag{3.51}$$

In this equation set, τ_η is the Kolmogorov timescale, $\mathcal{R}_\eta$ is the Kolmogorov Reynolds number, and u' represents the subgrid turbulence intensity.

Using the above formulation of the b-Xi 2-Equation model of Weller [52] XiFoam uses the following equations:

$$\frac{\partial}{\partial t}(\rho b) + \nabla(\rho\vec{u}b) - \nabla\cdot\left(\frac{\mu_t}{Sc_t}\nabla b\right) = -\rho S b \tag{3.52}$$

$$\mu = A_s\frac{\sqrt{T}}{1 + T_s/T} \tag{3.53}$$

$$\rho S b = \rho_u S_u \Xi|\nabla b| \tag{3.54}$$

$$\Xi = \frac{S_t}{S_u} = 1 + 2(1 - b)\left(0.62\sqrt{\frac{u'}{S_u}}R_\eta\right) \tag{3.55}$$

Constant turbulent Prandtl and Schmidt numbers are used to calculate turbulent diffusion terms. Here, S_u is the unstretched laminar flame speed, and Ξ stands for the flame wrinkling factor. u' is the turbulence intensity, which is computed from the turbulent kinetic energy using the isotropic turbulence hypothesis:

$$u' = \sqrt{2/3\,k} \tag{3.56}$$

The solver employs the variable specific heats calculated from JANAF tables which are defined separately for burned and unburned gases regions. The varying dynamic viscosity is calculated using Sutherland's law:

$$\mu = A_s \frac{T^{0.5}}{1 + T_s/T} \tag{3.57}$$

where $A_s = 1.67212e - 6$ and $T_s = 170.672$ are Sutherland model coefficients and T is the mixture temperature which varies in the domain.

The XiFoam solver does not solve any chemistry. The variables of c_p and mass fractions of reactants and products should be defined by the user. The c_p values for all fuel mixtures are calculated using "adiabaticFlameT" solver of OpenFOAM. This solver is not suitable for calculating hydrogenated mixtures; it only computes the pure fuel-air mixtures for common hydrocarbons. Therefore, the c_p values for hydrogenated cases are calculated using mass weighted averaging of species JANAF coefficients. The calculation method is presented as follows:

The equivalence ratio is calculated as:

$$\phi = \frac{\frac{m_{fuel}}{m_{oxidizer}}}{\left(\frac{m_{fuel}}{m_{oxidizer}}\right)_{stoich}} \tag{3.58}$$

The formula used in the calculations is from the Chemkin user manual [54], while c_p values are taken from Burcat [55]:

$$\frac{C_{p_k}^0}{R} = a_{1k} + a_{2k}T_k + a_{3k}T_k^2 + a_{4k}T_k^3 + a_{5k}T_k^4 \tag{3.59}$$

$$\overline{W} = \frac{\sum_{k=1}^{K}[X_k]W_k}{\sum_{k=1}^{K}[X_k]} \tag{3.60}$$

The calculated c_p values are presented in Figures 3.12 to 3.14.

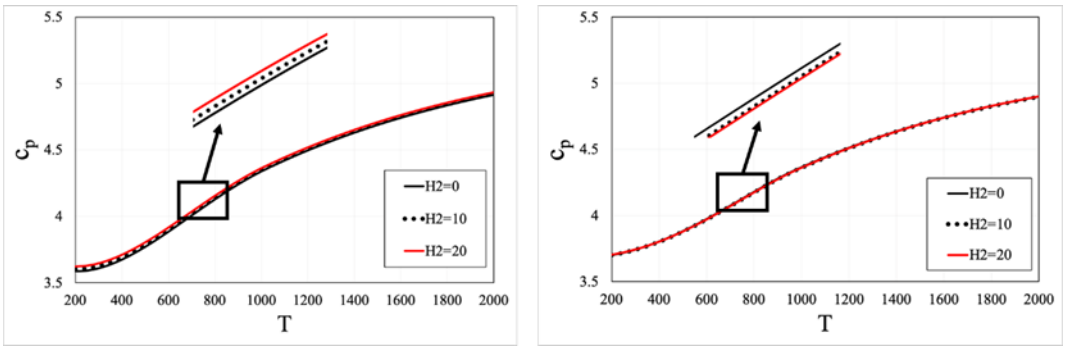

Figure 3.12. Calculated cp values for (left) Reactants (right) Products, for Φ=0.6

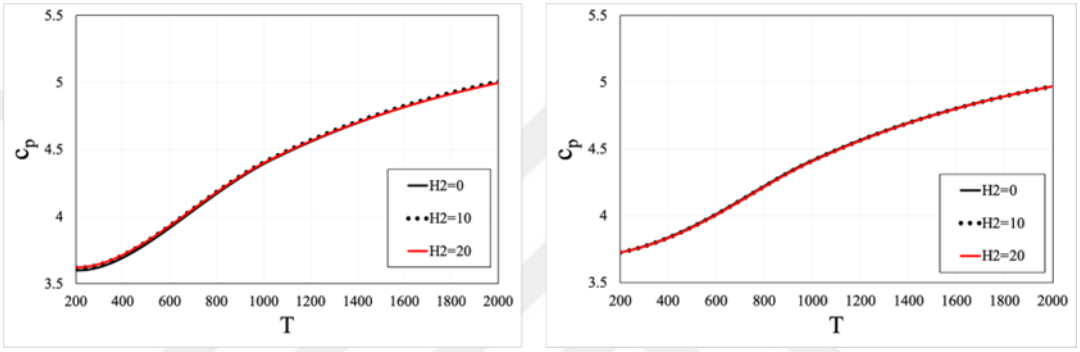

Figure 3.13. Calculated cp values for (left) Reactants (right) Products, for Φ=0.7

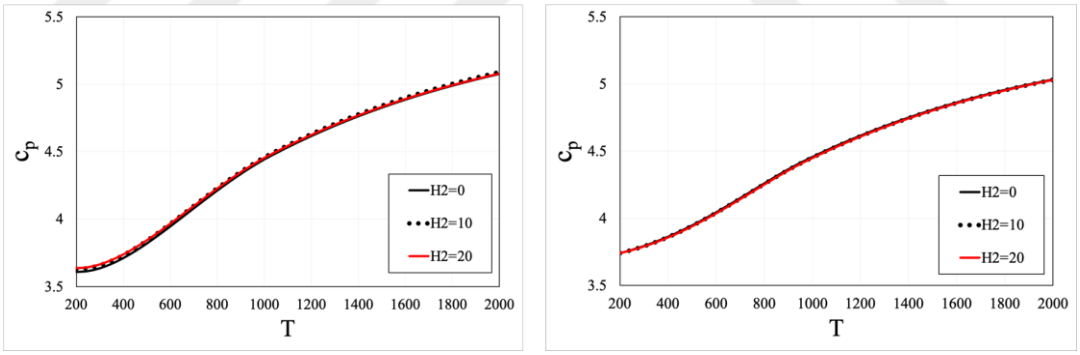

Figure 3.14. Calculated cp values for (left) Reactants (right) Products, for Φ=0.8

For a lean, premixed flame, the chemistry calculation system is a very stiff process since the enthalpy is very high. Therefore, the results would change even with small changes in c_p values. Although the c_p graphs follow nearly the same trends in each equivalence ratio case for three hydrogen addition rates, the small changes have a very large impact.

The reactants' mass fractions are calculated using the following mass fraction formula from Chemkin [54]:

$$Y_k = \frac{X_k W_k}{\sum_{j=1}^{K} X_j W_j} = \frac{X_k W_k}{\bar{W}} \tag{3.61}$$

Cantera solver is used for calculating the equilibrium species of burnt products by simulating a 1D premixed flame for each condition. The concentrations larger than 10^{-2} are selected for ease of calculation for the c_p calculations. The results are given in Tables 3.3 to 3.8.

Table 3.3. Mass fractions of reactant species for ϕ=0.6

	CH_4	H_2	O_2	N_2
0 [mol%]	0.0339	0	0.2251	0.7410
10 [mol%]	0.0330	0.0005	0.2252	0.7414
20 [mol%]	0.0319	0.0010	0.2253	0.7418

Table 3.4. Mass fractions of reactant species for ϕ=0.7

	CH_4	H_2	O_2	N_2
0 [mol%]	0.0393	0	0.2239	0.7369
10 [mol%]	0.0382	0.0005	0.2240	0.7373
20 [mol%]	0.0370	0.0008	0.2240	0.7375

Table 3.5. Mass fractions of reactant species for ϕ=0.8

	CH_4	H_2	O_2	N_2
0 [mol%]	0.0446	0	0.2226	0.7328
10 [mol%]	0.0435	0.0006	0.2227	0.7332
20 [mol%]	0.0421	0.0009	0.2228	0.7334

Table 3.6. Mass fractions of burnt species for ϕ=0.6

	CO_2	H_2O	O_2	N_2
0 [mol%]	0.0929	0.0760	0.0891	0.7403
10 [mol%]	0.0900	0.0777	0.0888	0.7416
20 [mol%]	0.0875	0.0805	0.0892	0.7410

Table 3.7. Mass fractions of burnt species for ϕ=0.7

	CO_2	H_2O	O_2	N_2
0 [mol%]	0.1076	0.0880	0.0656	0.7357
10 [mol%]	0.1048	0.0904	0.0656	0.7360
20 [mol%]	0.1014	0.0932	0.0656	0.7365

Table 3.8. Mass fractions of burnt species for ϕ=0.8

	CO_2	H_2O	O_2	N_2
0 [mol%]	0.1216	0.0996	0.0426	0.7312
10 [mol%]	0.1184	0.1023	0.0426	0.7316
20 [mol%]	0.1146	0.1055	0.0426	0.7321

The solver finally requires the unstretched laminar flame speed S_L. This is also calculated using CANTERA, with Grimech 3.0 mechanism. The changes of S_L with the equivalence ratio and the hydrogen addition rate are shown in Fig. 3.15.

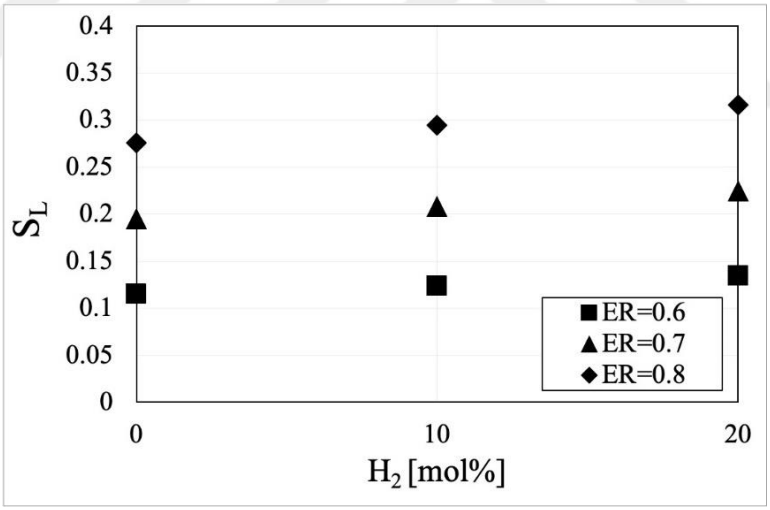

Figure 3.15. Laminar flame speed calculations for the experimental conditions

Hydrogen addition changes the Lewis number, and to investigate the effect of the Lewis number on flame wrinkling, the bi-Lewis model formulation is used to calculate a mixture Lewis number.

$$Le_{bi-fuel} = (1-\alpha)Le_{fuel\,A} + \alpha\, Le_{fuel\,B} \tag{3.62}$$

Here, α denotes the volume fraction of the second fuel B. The fuel Lewis numbers should be computed using the mass and thermal diffusivities of the fuels, and they are found as 0.955 for $\phi = 0.6$, 0.935 for $\phi = 0.7$, and 0.918 for $\phi = 0.8$ [56].

The boundary conditions are written for a cold, premixed fuel mixture entering the domain from the inlet region and a stoichiometric pilot flame entering the domain from the pilot region. As in the experiments, an ignition spark is modeled at 0.5 mm up from the pilot region, at a single point. The ignition is turned off after a stable flame is obtained. The domain is initially filled with air; the outlet condition is modeled as open to the atmosphere and the pressure inside the domain is atmospheric as in the experiments. The turbulence conditions are provided with the perforated plate inside the 3D numerical domain. To ensure computational stability, the maximum Courant number is set as 0.2. The initial and boundary conditions are summarized in Table 3.9.

Table 3.9. Initial and Boundary Conditions

Variable	Definition	Initial Conditions	Boundary Conditions			
			Inlet	Pilot	Outlet	Wall
S_u	Laminar flame speed [m/s]	uniform (Inlet S_u)	FV	FV	IO	ZG
T	Temperature [K]	uniform 300	FV	FV-burnt	IO	FV
T_u	Unburnt temperature [K]	uniform 300	FV	FV-burnt	IO	FV
U	Velocity Field [m/s]	uniform (0 0 0)	FV	FV	IO	FV 0
Xi	Wrinkling factor S_t/S_u (dimensionless)	uniform 1	FV	ZG	IO	ZG
alphat	Turbulence thermal diffusivity [kg/ms]	uniform 0	ZG	ZG	ZG	Wall Function
b	Regress variable (dimensionless)	uniform 1	FV 1	FV 0	IO 1	ZG
k	Turbulence kinetic energy m^2/s^2	uniform 2e-5	FV	FV	IO	ZG
nut	Turbulence viscosity [kg/m·s]	uniform 0	ZG	ZG	ZG	Wall Function
p	Pressure [kg/m·s^2]	uniform 100000	ZG	ZG	ZG	waveTransmissive

CHAPTER 4

RESULTS

The experimental and numerical results of this work are presented in this chapter. The numerical results are validated with the experimental flame height

4.1 Experimental Results

Chemiluminescence and laser induced Mie scattering results are presented below. The postprocessing methods are explained for each technique. The experimental flame conditions are summarized in Table 4.1, and the flame conditions are represented on the modified regime diagram in Fig. 4.1 (previously presented on Fig. 2.2). The integral length scale is assumed to be equal to perforated plate hole diameter, 2.5 mm.

Table 4.1. Turbulence characteristics of the experimental conditions

Φ	H_2 %	u' [m/s]	u'/S_L	δ_L [m/s]	I_0/S_L
0.6	0	0.15	1.299	0.975	2.563
	10	0.15	1.209	0.666	3.755
	20	0.16	1.186	0.534	4.686
0.7	0	0.15	0.768	0.924	2.706
	10	0.15	0.720	0.637	3.928
	20	0.16	0.713	0.513	4.877
0.8	0	0.15	0.543	0.866	2.887
	10	0.15	0.510	0.605	4.132
	20	0.16	0.506	0.490	5.100

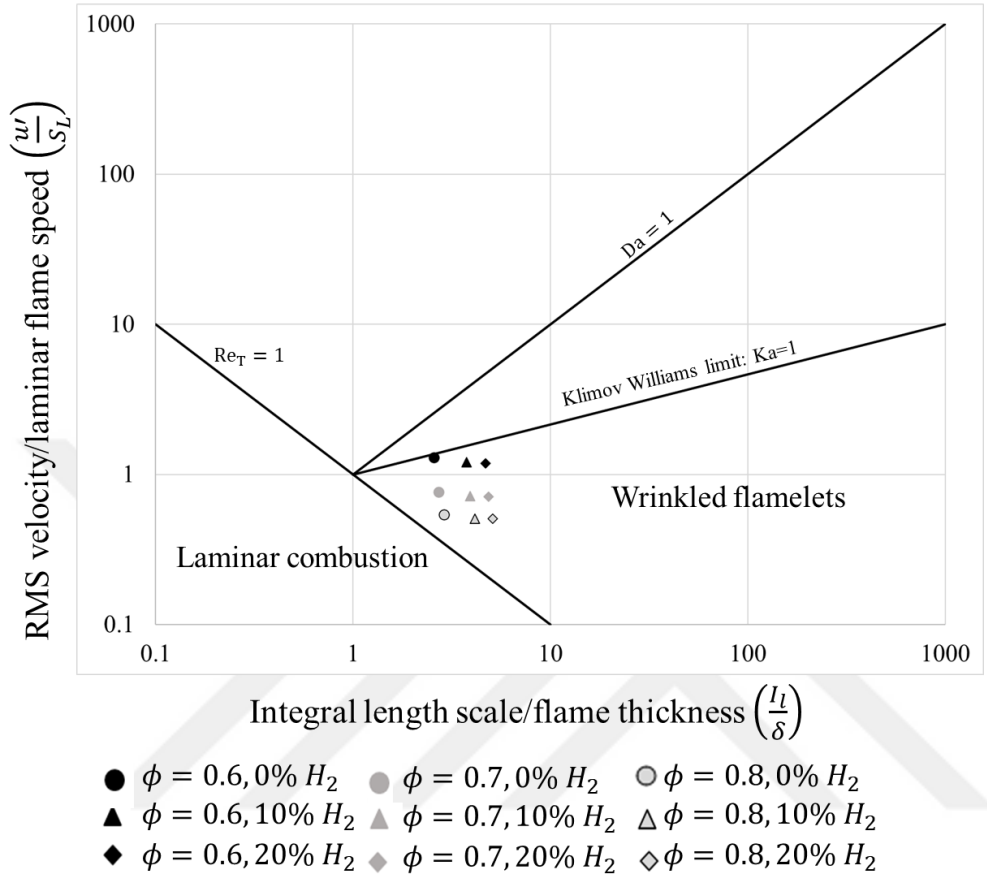

Figure 4.1. Experimental conditions on regime diagram

As seen in the table and the figure, all the flames that we investigated are in the wrinkled flamelets regime.

4.1.1 Chemiluminescence Results

Since chemiluminescence measurements provide line-of-sight measurements, the inverse Abel transform is performed to recover 2D images from 3D images, using the Fourier-based Abel inversion technique [57]. The raw chemiluminescence images are first scaled and cropped. For postprocessing, the images are binarized, adjusted, and filtered using a Wiener filter to capture the luminous areas in the image. The pilot flame is cropped in every test case to prevent the effect of this

stoichiometric flame luminosity on the CH* and OH* signals. Instantaneous turbulent flame fronts (flamelets) are not symmetric by nature. Therefore, first, the intensity at every pixel is calculated, then the luminous zone weighted center is found and assumed to be the flame center. The flame center is used for averaging radially the images, to create an axially symmetric image that is suitable for Abel Transform. The image is cropped to account for the imaging window, which is 10 cm in total. The imaging window size is determined as the window size. Using a Fourier series expansion of 40 expansions in an integral part, the inverse Abel transform integral is calculated [58-59]. The inverse Abel transform procedure is summarized in Figs. 4.2.

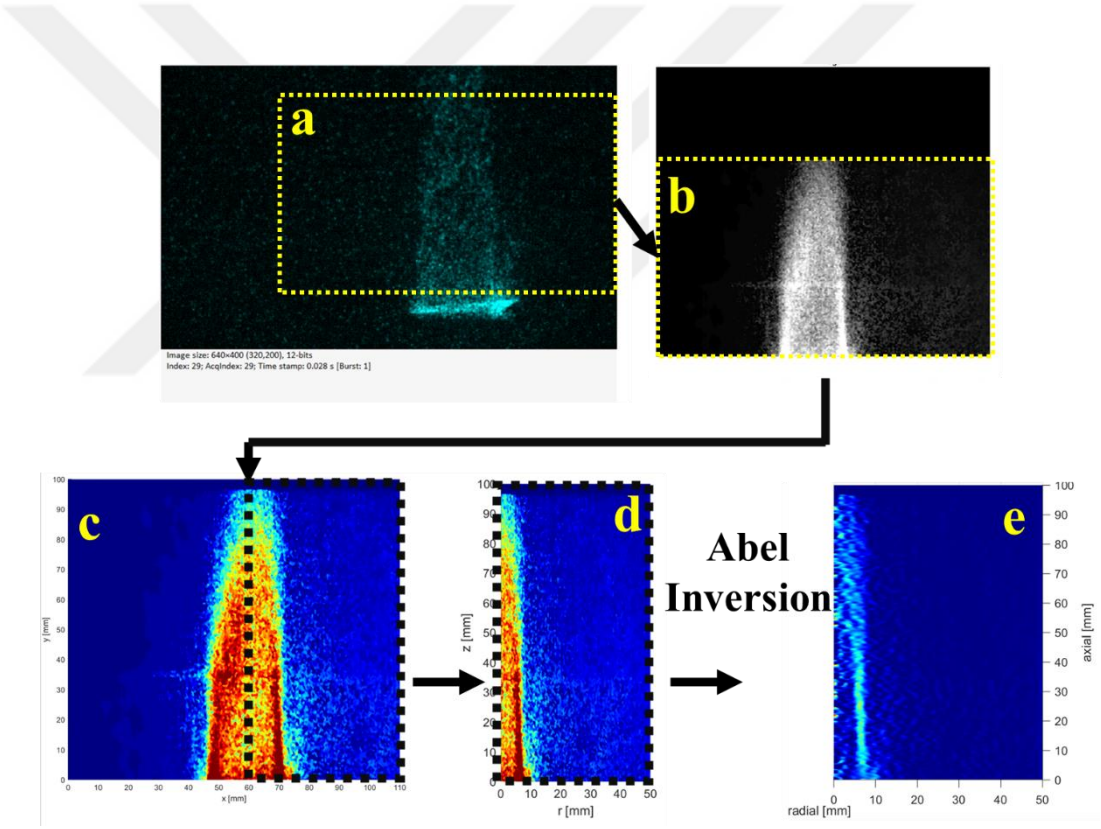

Figure 4.2. The Abel inversion procedure, (a) The raw chemiluminescence image, (b) Grayscale averaged and cropped image (c) Symmetric chemiluminescence intensity with respect to image center (d) Half of the flame for averaging (e) Inverse Abel transformed and normalized image

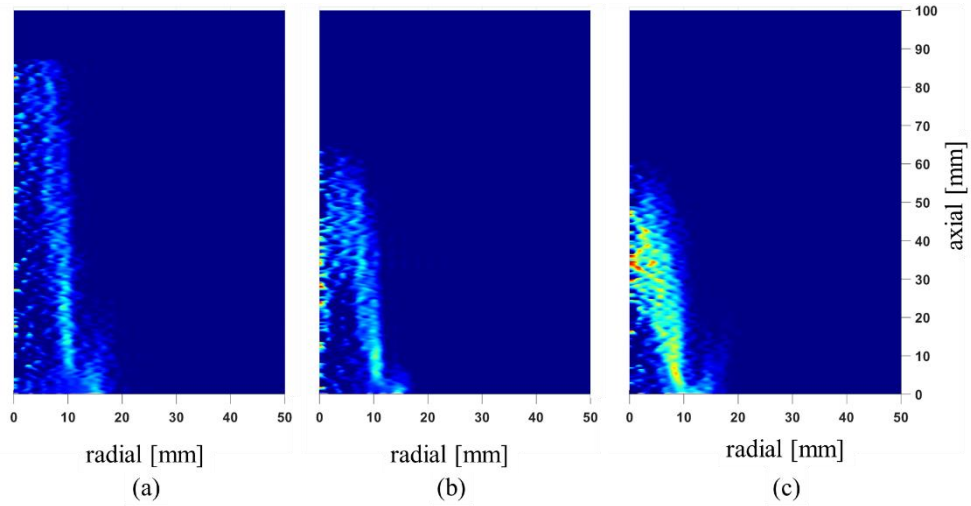

Figure 4.3. Normalized inverse Abel transformed intensity figures of CH* for ϕ=0.6 for (a) 0%, (b) 10, (c) 20% of H2 addition

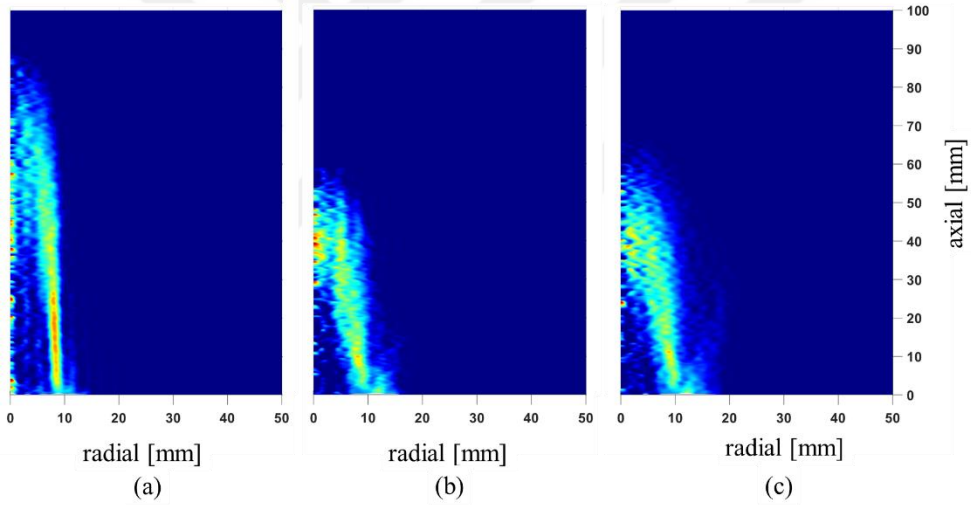

Figure 4.4. Normalized inverse Abel transformed CH* intensity figures for ϕ=0.7 (a) 0%, (b) 10%, (c) 20% of H2 addition

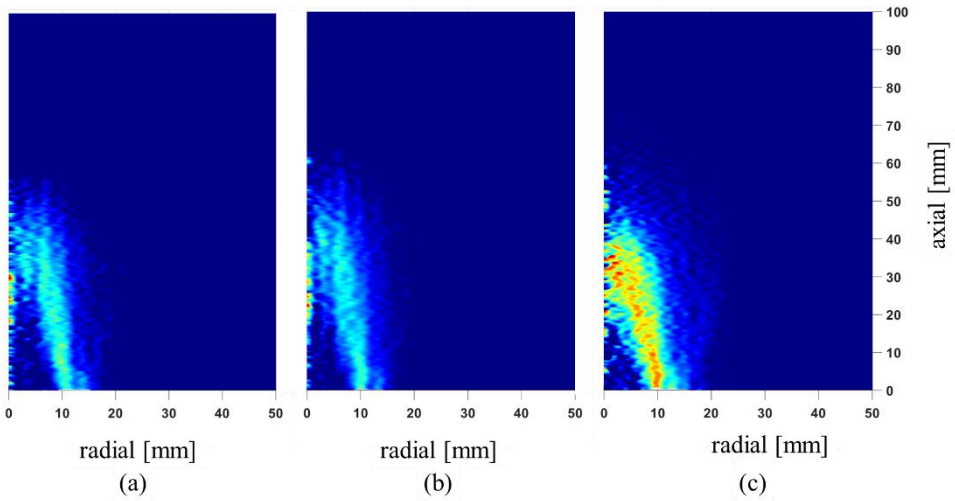

Figure 4.5. Normalized inverse Abel transformed CH* intensity figures for ϕ=0.8. (a) 0%, (b) 10%, (c) 20% of H2 addition

The inverse Abel transformed images show the effect of hydrogen addition clearly on flame height. As hydrogen is added to the premixture, flame height strongly decreases. The equivalence ratio increases results in decreasing the flame height as well. For all equivalence ratio cases, the increase in hydrogen content results in the increase of light intensity in the figures, which is a natural consequence of the increased hydrogen affecting the CH* production.

Chemiluminescence images of OH* and CH* radicals are compared in Fig. 4.6. As the hydrogen addition rate increases, the light intensity of OH* radicals change significantly, while CH* intensity is not significantly changing with the overall flame structure changes. This is another reason why we have chosen CH* radicals for indicating the flame surface.

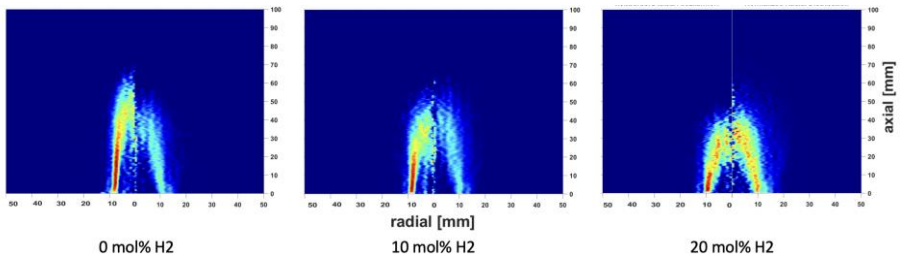

Figure 4.6. Normalized radial intensity for OH* (right) and CH* (left) values for ϕ = 0.8 and various H2 addition rates

4.1.1.1 Turbulent Flame Speed

The chemiluminescence measurements were used to calculate the turbulent flame speed using the cone approach for Bunsen burners [47, 60-61]. Here, the CH* images were used to represent the progress variable c. The CH* images were normalized between 0 and 1, creating a progress variable (c) contour. The reference cone surface is selected as c=0.5. The turbulent flame speed is calculated using Eq. 4.1, where R is the burner radius, U is the mean inlet velocity and H is the reference surface height constructing the cone.

$$S_T = \sqrt{U^2/(1+(H/R)^2)} \tag{4.1}$$

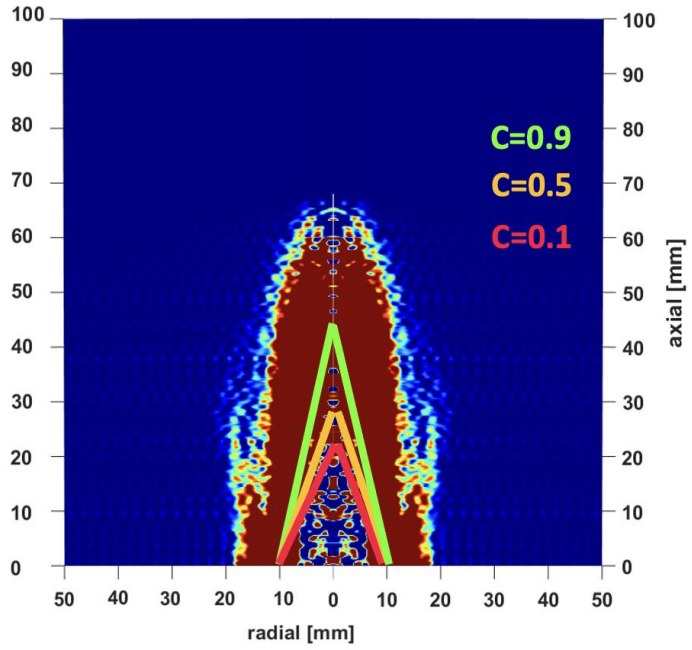

Figure 4.7. The cones for turbulent flame speed calculation

The turbulent flame propagation speed for various hydrogen rates and equivalence ratio values are given in Fig. 4.8. The same results normalized by the corresponding S_L values are shown in Fig. 4.9.

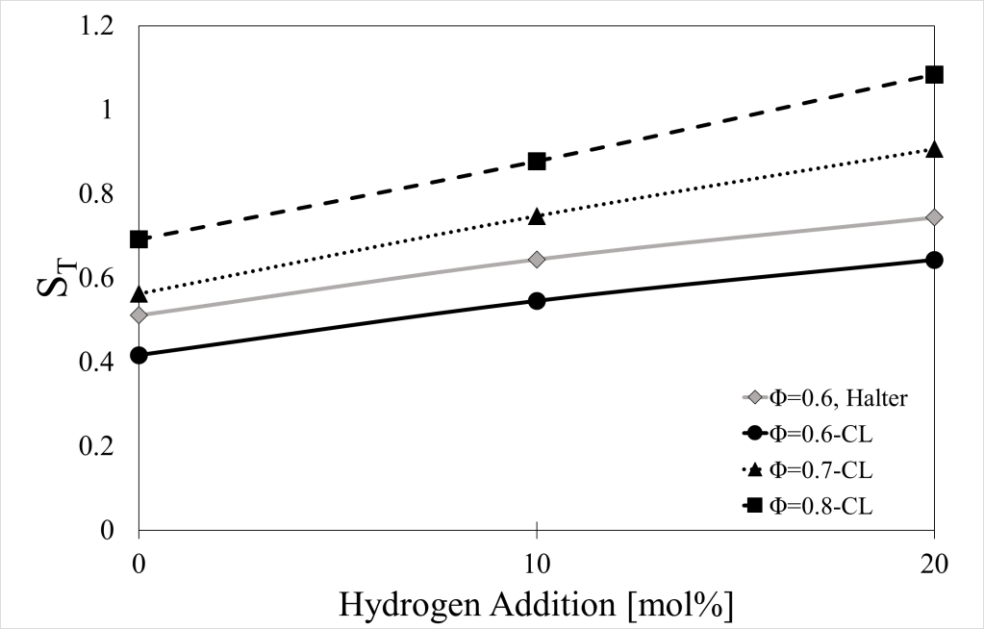

Figure 4.8. Turbulent flame speed from Chemiluminescence measurements

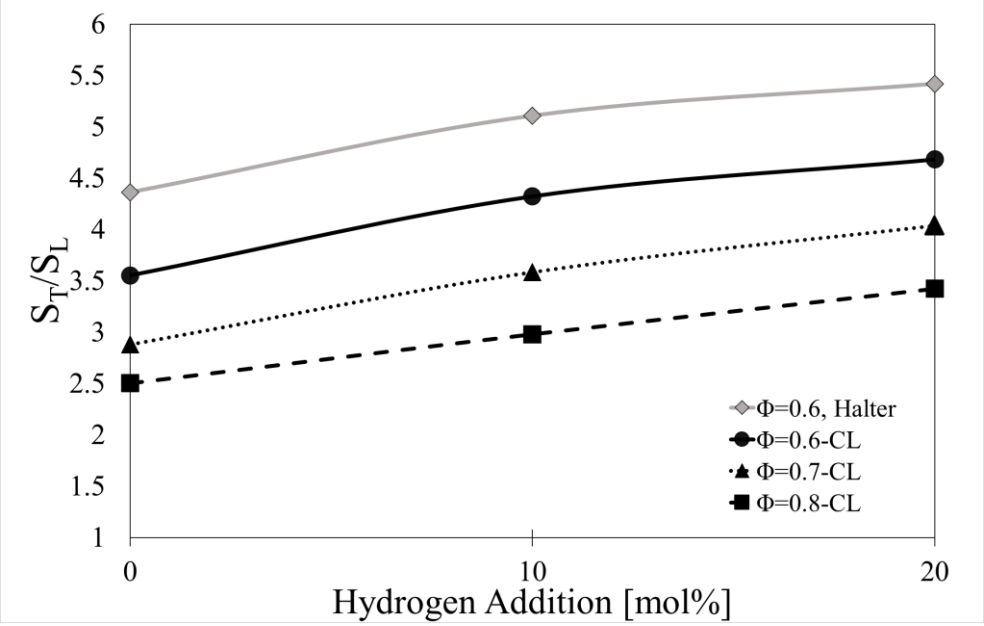

Figure 4.9. Normalized turbulent flame speed from chemiluminescence measurements

In Fig. 4.8, the S_T calculations from chemiluminescence images reveal that S_T increases both with the equivalence ratio and the hydrogen addition rate, which agrees with previous literature results of Halter et al. for $\phi = 0.6$ [47], who also

used the same cone method for calculating S_T . In Fig. 4.9, where S_T is normalized by S_L, the vertical ordering of the curves with respect to the equivalence ratio is reversed. This indicates that S_L increases more with both parameters compared to S_T.

4.1.2 Laser Induced Mie Scattering Results

Using Mie scattering tomography results, instantaneous flame front tracking is performed with MATLAB. The snapshots are averaged for 500 images for each case, binarized, and dilated to generate a clean binarized image. The flame front is then filtered with Gaussian and Wiener filters. The image is finally segmented. The instantaneous flame front is collected for 50 images per case, and the instantaneous flame fronts are superimposed [60]. The images are used to determine the turbulent flame speed.

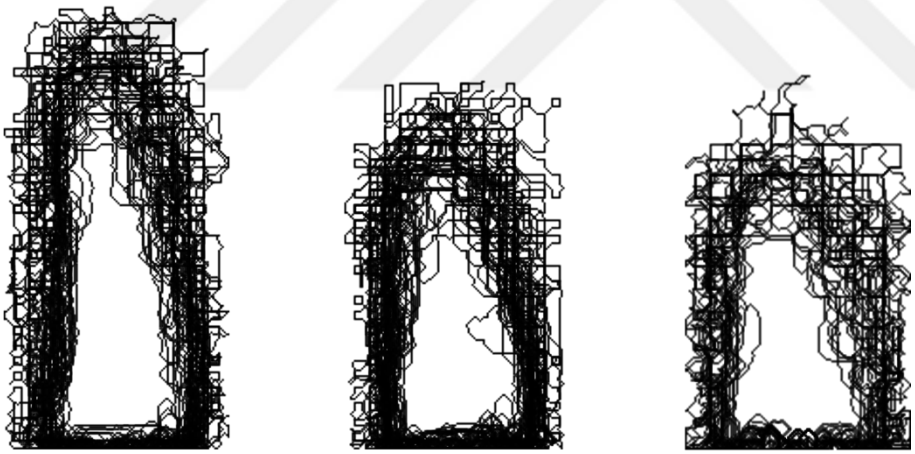

Figure 4.10. Flame brush for $\phi = 0.6$

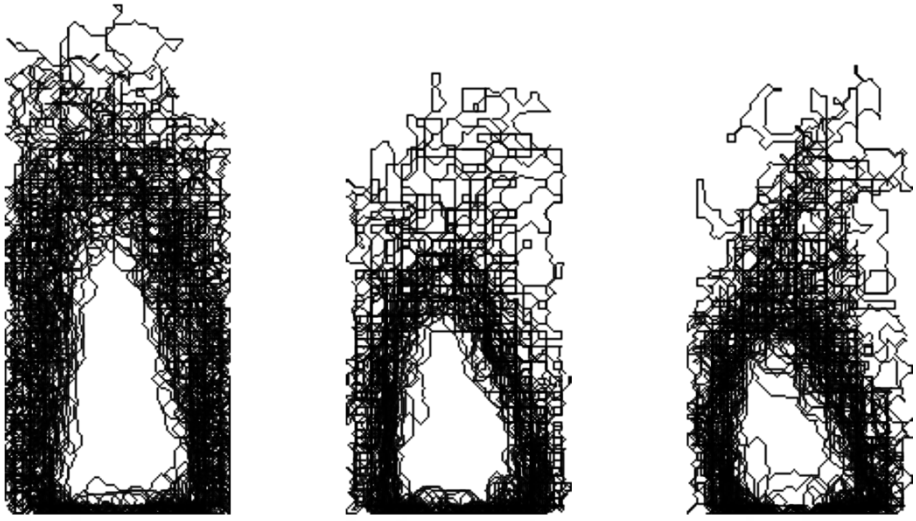

Figure 4.11. Flame brush for $\phi = 0.7$

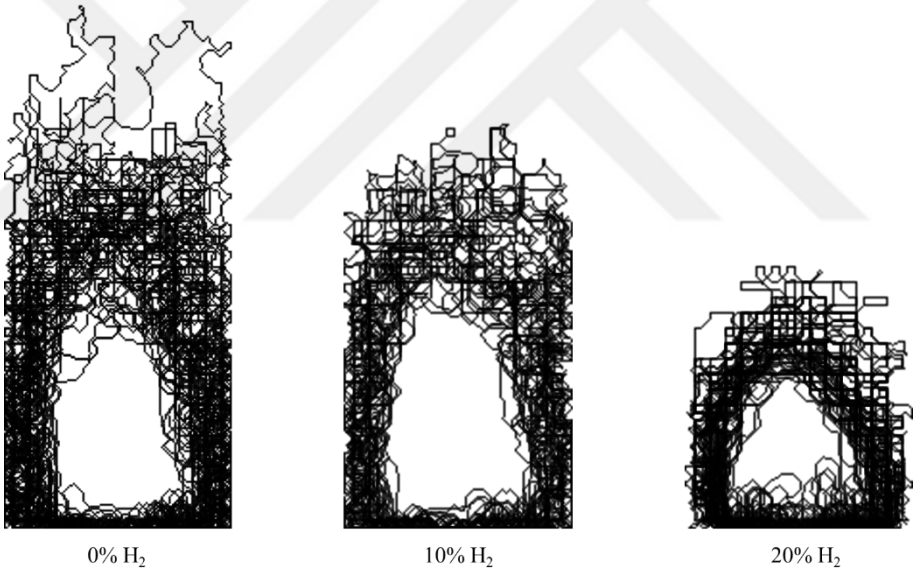

Figure 4.12. Flame brush for $\phi = 0.8$

Figs. 4.10-4.12 represent the superposition of instantaneous flamelets for all the experimental cases. The average flame brushes clearly show the shortening of the turbulent flames both on the unburnt and burnt sides, with increasing equivalence ratio and hydrogen addition rates. The leanest case has a narrower and long shape compared to the richest and highest hydrogen addition rate case.

Mie scattering images are post processed to determine the turbulent flame propagation speed. Mie scattering images are averaged and, c=0.1 and c=0.9 contours are determined, assuming the unburnt side of the flame corresponds to c=0.1, while the burnt limit of the flame corresponds to c=0.9. The flame brush is then divided into 9 equal parts to find the c=0.5 contour. C=0.5 contour is used to calculate the turbulent flame speed. The process is shown for ϕ=0.6 case in Figure 4.13 as an example.

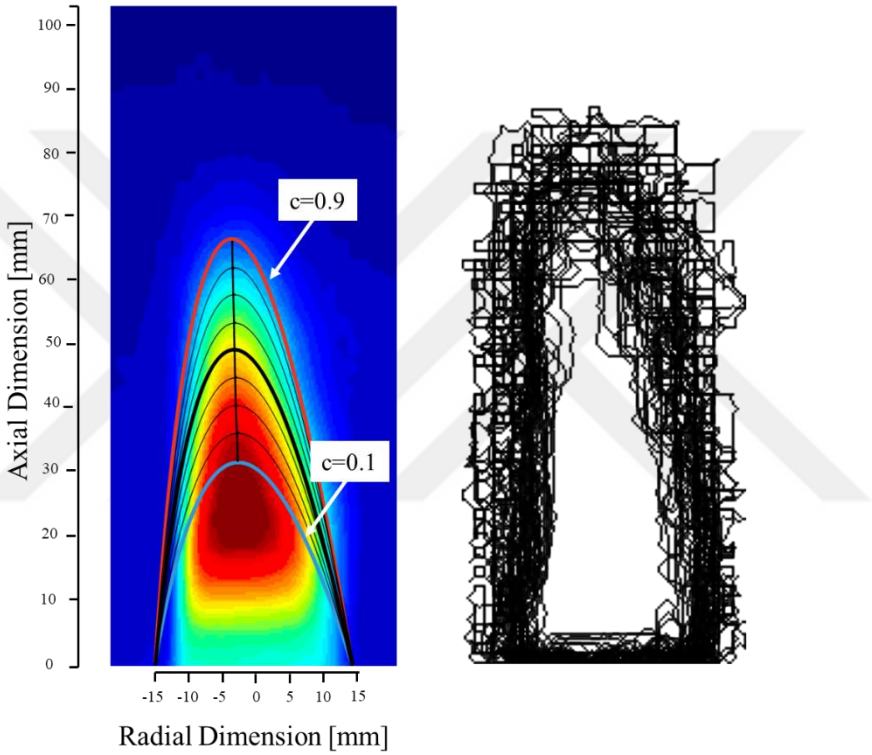

Figure 4.13. Flame brush and progress variable calculations

The c=0.5 curve is used for calculating the turbulent flame propagation speed by using the same cone method as in the chemiluminescence measurements. The turbulent flame speed calculations from the Mie scattering experiments are provided in Figs.4.14 and 4.15.

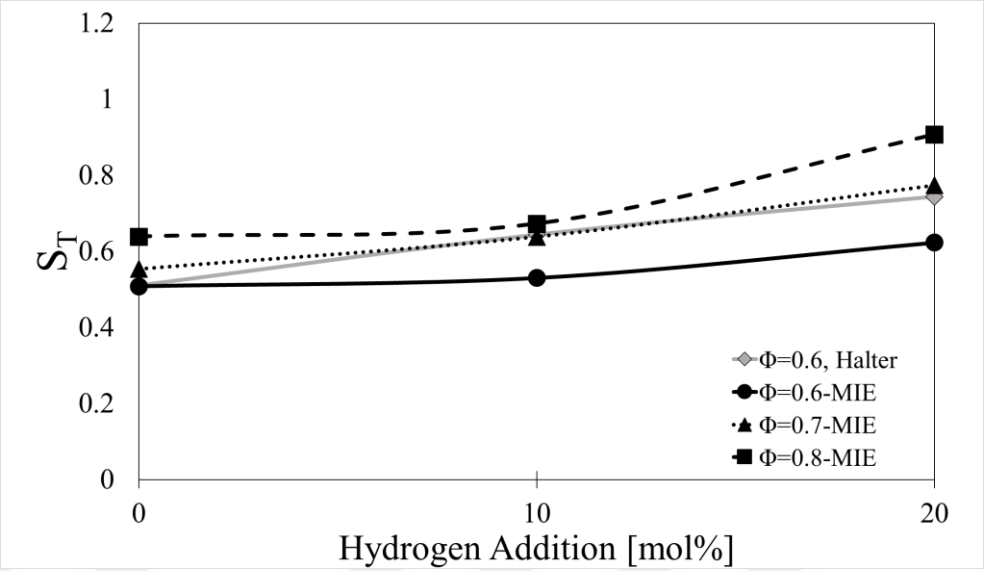

Figure 4.14. Turbulent flame speed calculations from Mie scattering measurements

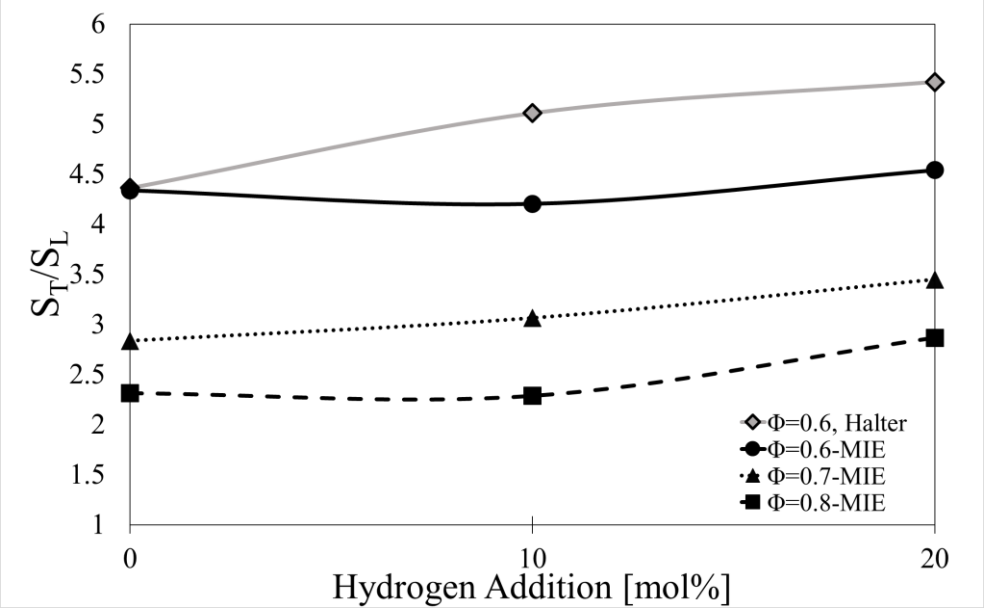

Figure 4.15. Normalized turbulent flame propagation speed from Mie scattering measurements

The turbulent flame speed values from MIE and CL experiments are close to each other, with CL measurements are almost always higher than MIE results. The deviation may be caused by the line-of-sight measurements in chemiluminescence

and a more precise description of the 2D images by the Mie scattering technique. Fig. 4.16 represents the calculated S_T values from both experiments, while Fig. 4.17 shows the turbulent flame speed of CL measurements ($S_{T,CL}$) normalized by the turbulent flame speed of MIE measurements ($S_{T,MIE}$). The plot gives an insight about how both methods are close to each other, by scattering around a ratio equal to 1. We also observe that the increasing hydrogen addition rate has the effect of forcing the $S_{T,CL}$/ $S_{T,MIE}$ ratio closer to 1. This may be due to the increase in the radical emissions with hydrogen addition to the premixture. Increased emissions may result in clearer line-of-sight images, which provide a better picture of inverse Abel transformed 2D images and more accurate S_T values. In any case, it is satisfactory that the two techniques can be interchangeably used to estimate this major parameter for turbulent premixed flames, S_T, so that depending on the combustor and flame configurations, both laser and less complex chemiluminescence techniques can be used.

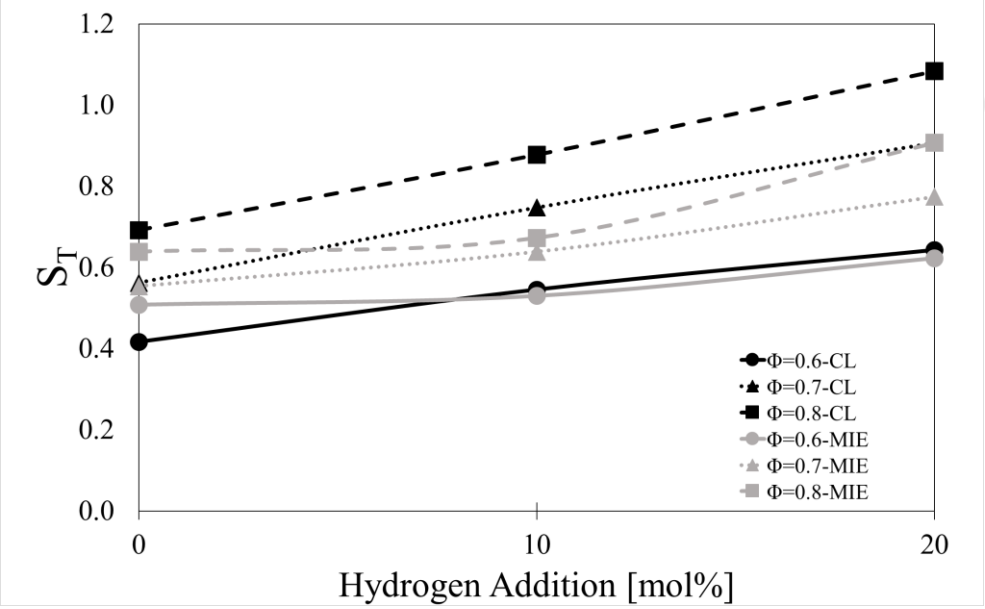

Figure 4.16. Turbulent Flame Speed calculated from chemiluminescence and Mie scattering experiments

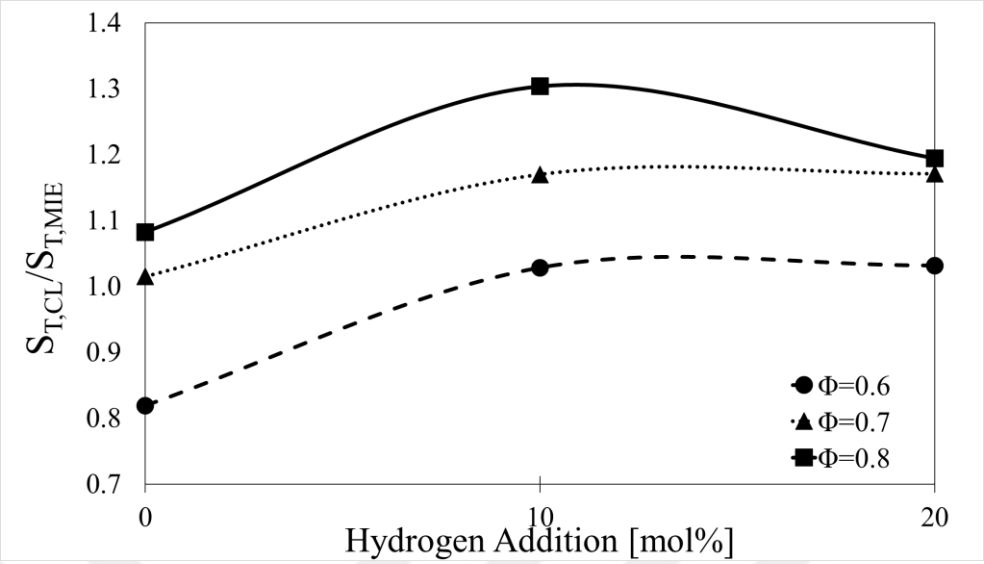

Figure 4.17. The ratio of the turbulence flame speeds calculated from chemiluminescence (CL) and Mie scattering (MIE) experiments

Flame brush thicknesses are measured as the maximum spatial distance from c=0.1 to c=0.9 on the burner vertical axis. The values are presented in Table 4.1.

Table 4.2. Flame brush thicknesses from Mie Scattering experiments

ϕ	H_2 [mol%]	Flame Brush Thickness [mm]
$\phi = 0.6$	0	36
	10	28
	20	23
$\phi = 0.7$	0	31
	10	20
	20	17
$\phi = 0.8$	0	22
	10	19
	20	16

The flame brush thickness decreases when with the increase of both the equivalence ratio and the hydrogen addition rate. The turbulent brush thickness is previously mentioned to depend mainly on flame wrinkling [62]. According to Attili et al [63], flame brush thickening is associated with relatively big and intermittent turbulent structures [32] that have enough energy to change the inner flame thickness without

considerably slowing down the reaction rate. The length scales are therefore further investigated in our numerical simulations to observe such effects.

4.1.3 Flame Front Curvature Distributions

Mie scattering images are used to determine the distribution of flame front curvatures. The postprocessing steps are explained in Figs. 4.18. First, the flame front is tracked using the exterior boundaries of the binarized image as shown in Fig. 4.18 (a). The flame front is also recorded by fitting a B-Spline curve to the boundary; therefore, the flame front location could be stored inside an x-y matrix Fig. 4.18 (b). The stored B-Spline curve is divided into equal distance points, such that the linear distance between consecutive points is equal to 5 mm, where this distance is decided by a trial and error process. Next, for every 3 points, a circle is fitted, and the radius values of the circles are determined, as it is explained in Chapter 2.3. The cross product of the vectors formed by the 3 points is used to decide if the curvature is convex or concave for the sign of the curvature. The curvature is found using the relation $\kappa=1/r$, where r is the radius of the fitted circle and K is the curvature, by using Eqn. 2.1.

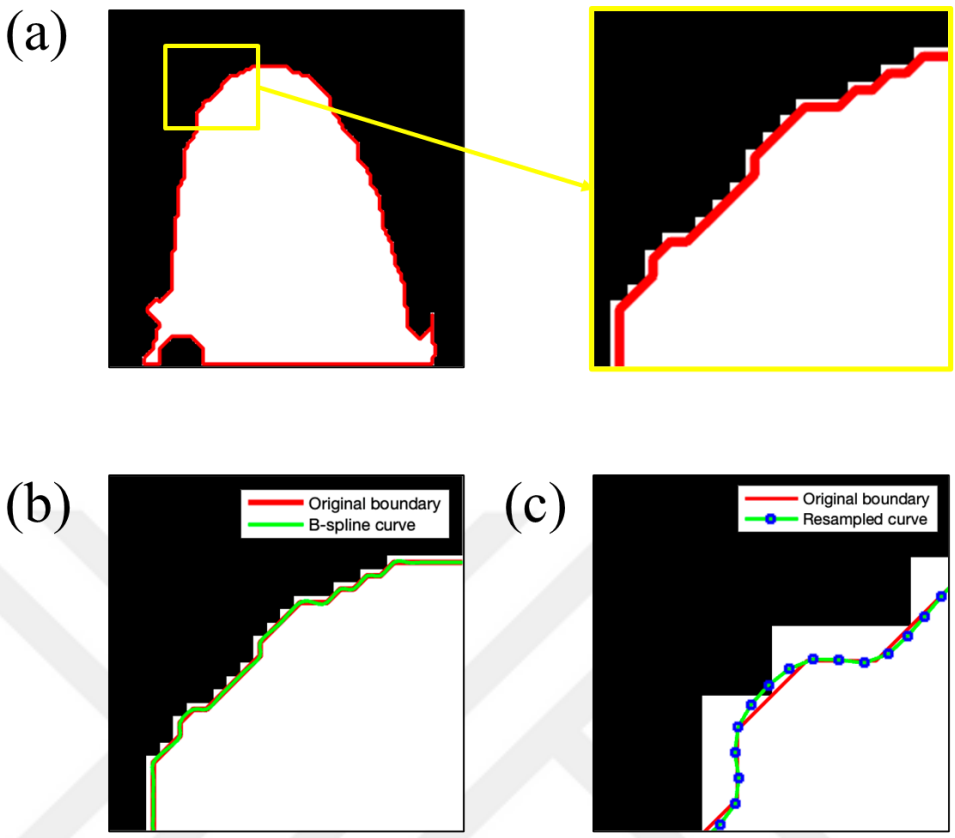

Figure 4.18. (a) Boundary tracking (b) B-Spline curve (c) Divided spline

The averaged Mie scattering images are finally used to observe the flame compactness. For this aim, L/D ratio of the flame is used, where L refers to the flame height and D is the burner diameter. The L/D ratio is presented in Fig. 4.19 for ϕ=0.7 flame with various hydrogen addition rates, showing a clear decrease in flame height with hydrogen addition.

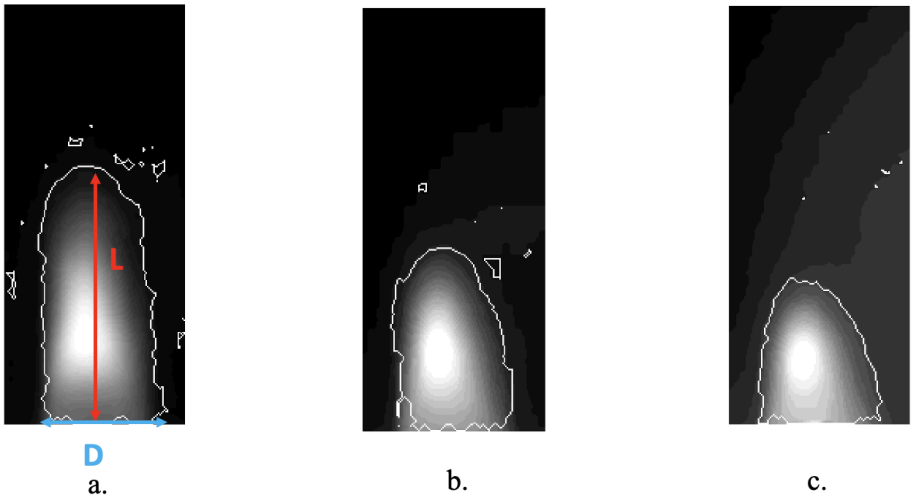

Figure 4.19. Flame front identification for ϕ=0.7 (a) 0% H_2, (b) 10% H_2, (c) 20% H_2

Table 4.3. L/D ratio for the experimental matrix

H_2 [mol%]	0	10	20
$\phi = 0.6$	2.5	1.83	1.66
$\phi = 0.7$	2.16	1.8	1.2
$\phi = 0.8$	1.83	1.5	1.05

As shown in Table 4.3, the flame height is found to be decreasing with both the equivalence ratio increase and added hydrogen content to the mixture. Judging by the results, hydrogen has a compaction effect on the flame.

The curvature distributions probability density functions are calculated for each case using the default pdf function of MATLAB. The range is decided to cover the maximum and minimum values of all cases, and the number of points is decided to be the square root of the curvature datapoint number, as 100. The data point number is decided at the end of an iterative process. The probability density function graphs for all cases are provided in Figs. 4.20-4.22. All the PDFs are centered around their mean values and follow the normal distribution.

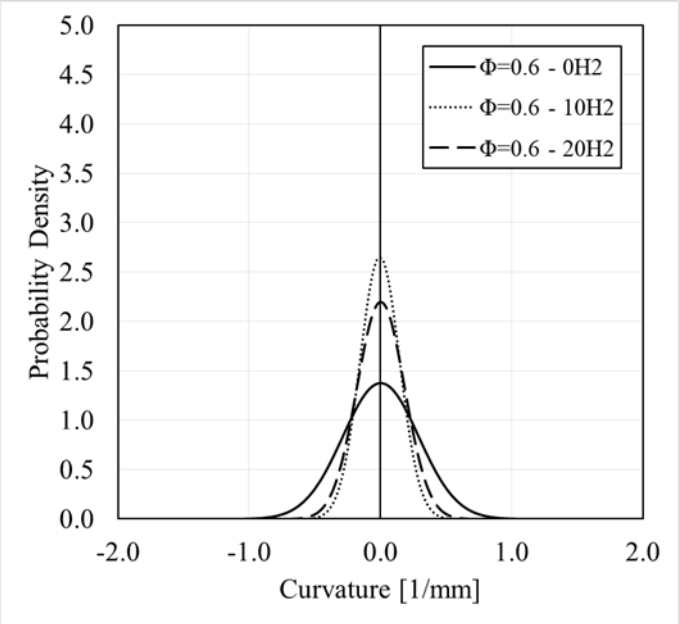

Figure 4.20. Curvature PDF for Φ=0.6

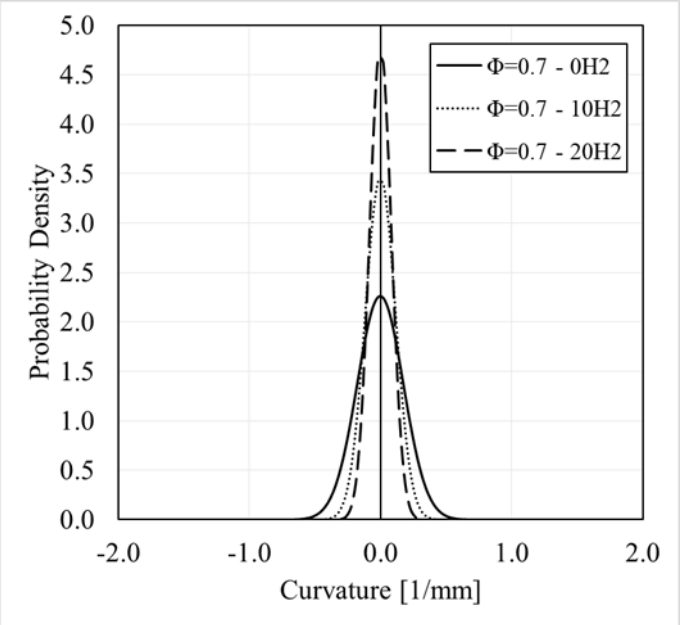

Figure 4.21. Curvature PDF for Φ=0.7

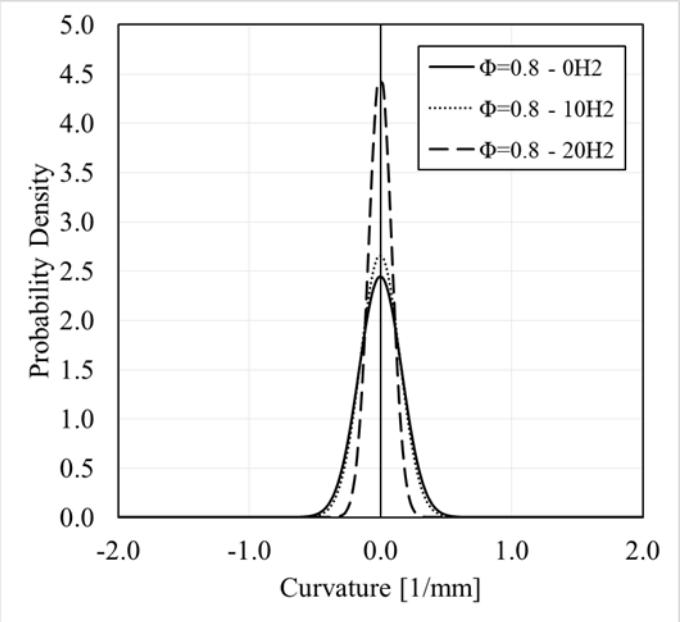

Figure 4.22. Curvature PDF for Φ=0.8

These results show that curvature distribution PDFs become narrower with increasing equivalence ratio, indicating that the probability of large curvatures decreases. This implies that the probability of small scale flame front wrinkles equally decreases. The same observation can also be made for a constant equivalence ratio when the hydrogen addition rate increases. Therefore, both increasing the equivalence ratio and increasing the hydrogen content of the mixture erase the smallest flame front wrinkles, and the instantaneous flame fronts become dominated by large scale surface wrinkles. If we recall that the increase of the equivalence ratio in lean flames and that of the hydrogen content of the lean mixture both reduce the instantaneous flame thickness, it appears that there is a challenging research area in order to investigate in more detail the relationship between the flame surface wrinkles topology and the instantaneous flame front structure and thickness. We may recall here that in [40], it is claimed that hydrogen addition to methane-air turbulent flames generates smaller instantaneous flame front wrinkles, in opposition to the results presented here. This shows that additional investigations are needed to progress in this important issue. We hope to answer such questions by applying the

laser induced Rayleigh scattering technique in our future work together with advanced numerical simulations of the premixed flame front dynamics and structure.

4.2 Validation of Numerical Studies with Experiments

The numerical results are compared to the experiments. The mean progress variable cMean is used as the comparison parameter.

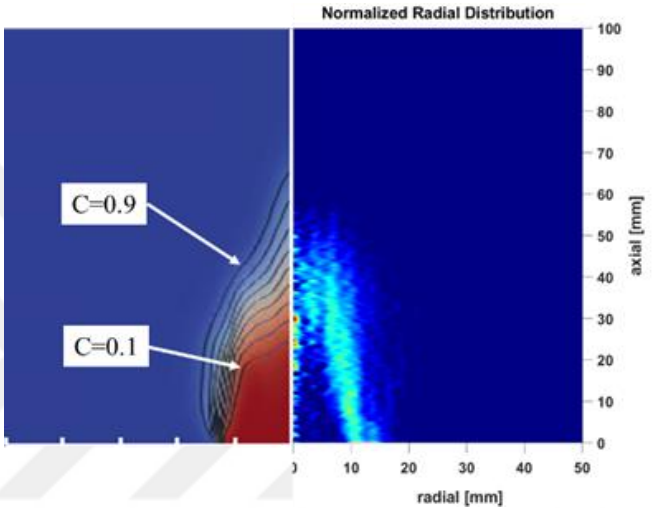

Figure 4.23. Φ=0.8, 0H2. Left is the progress variable and right is the CH* CL image

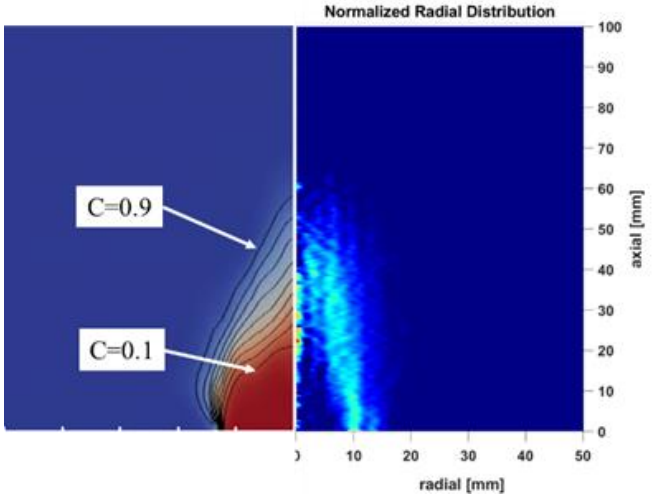

Figure 4.24. Φ=0.8, 10H2. Left is the progress variable and right is the CH* CL image

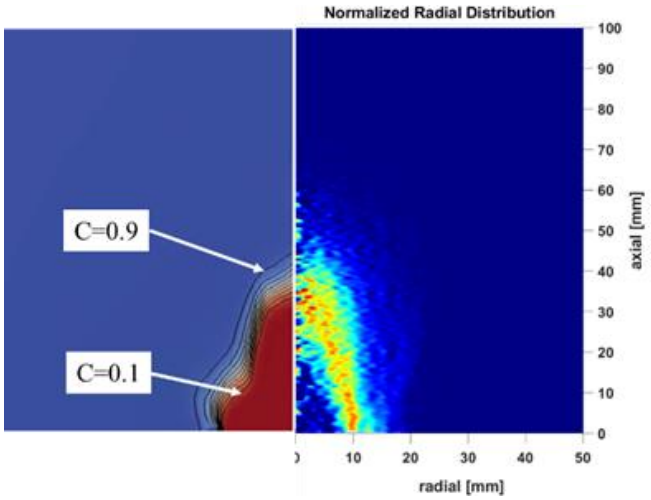

Figure 4.25. Φ=0.8, 10H2. Left is the progress variable and right is the CH* CL image

In Figures 4.23 – 4.25, the numerical simulations show the temperature field on the left side with progress variable c contours fitted from c=0.1 to c=0.9, and Abel inverted chemiluminescence results on the right side for $\phi = 0.8$. The chemiluminescence emissions were assumed to correspond to the same progress variable interval. There are differences between the numerical and experimental results, which may be caused by the Abel inversion procedure, burner angle, or the mean progress variable calculations. Judging by the error margins between the height measurements, the computations are considered to validate the experimental data. Table 4.4 presents the quantitative flame height data for both experimental methods and computations. It is generally observed that flame heights from the two experimental techniques are close to each other with some differences, the Mie scattering results showing higher flame height values. For both techniques, the results show that flame heights decrease both with the equivalence ratio and the hydrogen addition rate, due obviously to the increased reactivity of the mixture when these parameters increase.

Table 4.4. Flame heights calculated from Chemiluminescence (CL), Mie scattering (MIE) and numerical (Xi) results

ϕ	H_2 [mol%]	CL [mm]	MIE [mm]	XI [mm]	XI Errors	
					XI - CL [%]	XI -MIE [%]
$\phi = 0.6$	0	55.6	45.0	60	7.3	25.0
	10	41.7	43.0	53.1	21.5	19.0
	20	34.8	36.0	48.7	28.5	26.1
$\phi = 0.7$	0	40.3	41.0	35.4	-13.8	-15.8
	10	29.2	35.0	27.6	-5.8	-26.8
	20	23.0	28.0	34.8	33.9	19.5
$\phi = 0.8$	0	29.2	35.0	34.6	15.6	-1.2
	10	24.0	33.0	24.8	3.2	-33.1
	20	18.0	23.0	38.1	52.8	39.6

CHAPTER 5

CONCLUSIONS

The effects of hydrogen addition and equivalence ratio in lean premixed turbulent methane-hydrogen-air flames are studied experimentally and numerically. A high-pressure combustion chamber working between 0.1 MPa-0.9 MPa is installed and validated with a turbulent Bunsen burner, while the present experiments concern only atmospheric conditions.

The chemiluminescence and Mie scattering imaging techniques are used for the measurements. The chemiluminescence results are processed using inverse Abel transformation to convert the line-of-sight images, and the Mie scattering results are used to calculate flame curvature distributions and flame brush investigations.

The light intensity of the chemiluminescence of radicals increases with the hydrogen addition rate. With increasing hydrogen addition rate, the flame height is found to be decreasing while the normalized turbulent flame speed increases.

The turbulent flame speed calculated with Mie scattering data showed good agreement with the CL results, while the Mie scattering S_T values were generally lower than the CL data. This may be related to the line-of-sight measurements from the CL method and 2D measurements with Mie scattering.

The experimental conditions are numerically simulated with the XiFoam solver with the Large Eddy Simulation approach. The LES results are validated in this thesis with the flame height data from the experiments. The numerical framework we developed can now be used to calculate flame properties that are not attainable from the experiments, such as the flame surface density. The XiFoam results can also be used to investigate the effects of turbulence properties on the flame, such as the u'/S_L ratio.

Future work will include the high pressure operation of the combustion chamber and the investigation of the pressure effects on natural gas-hydrogen-air turbulent premixed flames. The perforated plate we used in this study will be replaced by other turbulence promoter plates having different blockage ratios and grid characteristics to investigate the turbulence effects combined with the high pressure effects. Finally, the instantaneous flame structures will be investigated by the laser induced Rayleigh scattering technique to better analyze the relationships between the instantaneous flame topologies and the flame thickness.

REFERENCES

[1] Wiatros-Motyka, M. (2023). (rep.). Global Electricity Review 2023. EMBER.

[2] Turns, S. R. (2021). An introduction to combustion: Concepts and applications. McGraw-Hill.

[3] Warnatz, J., Maas, U., Dibble, R. W. (1999). Combustion: Physical and Chemical Fundamentals, modeling and simulation, experiments, Pollutant Formation. Springer.

[4] F. Halter, "Caractérisation des effets de l'ajout d'hydrogène et de la haute pression dans les flammes turbulentes de prémélange méthane/air." [Online]. Available: https://tel.archives-ouvertes.fr/tel-00591421

[5] T. Lachaux, "Etude des effets de la haute pression sur la structure et la dynamique des flammes turbulentes de prémélange pauvre de méthane-air," Université d'Orléans, 2004. [Online]. Available: https://tel.archives-ouvertes.fr/tel-00010401

[6] R A. Libby and E A. Williams, Turbulent Reacting Flows. Berlin, New York: Springer-Verlag, 1980.

[7] A. N. Lipatnikov and V. A. Sabelnikov, "Karlovitz Numbers and Premixed Turbulent Combustion Regimes for Complex-Chemistry Flames," Energies, vol. 15, no. 16. MDPI, Aug. 01, 2022. doi: 10.3390/en15165840

[8] A. N. Kolmogorov, "The local structure of turbulence in incompressible viscous fluid for very large Reynolds numbers," Proc R Soc Lond A Math Phys Sci, vol. 434, no. 1890, pp. 9–13, Jul. 1991, doi: 10.1098/rspa.1991.0075.

[9] Damköhler, G. (1947). The effect of turbulence on the flame velocity in gas mixtures. Zeitschrift fuer Elektrochemie und Angewandte Physikalische Chemiw, 46(NACA-TM-1112).

[10] T. Poinsot and D. Veynante, Theoretical and Numerical Combustion, 3rd ed. 2012

[11] Peters, N. (1988, January). Laminar flamelet concepts in turbulent combustion. In Symposium (International) on combustion (Vol. 21, No. 1, pp. 1231-1250). Elsevier.

[12] Peters, N. (1999). The turbulent burning velocity for large-scale and small-scale turbulence. Journal of Fluid mechanics, 384, 107-132. [13] F. A. Williams, "An approach to turbulent flame theory," 1970.

[14] K. N. C. Bray and P. A. Libby, "Interaction effects in turbulent premixed flames," Physics of Fluids, vol. 19, no. 11, pp. 1687–1701, 1976, doi: 10.1063/1.861384

[15] B. Karlovitz, D. W. Denniston, and F. E. Wells, "Investigation of turbulent flames," J Chem Phys, vol. 19, no. 5, pp. 541–547, 1951, doi: 10.1063/1.1748289

[16] Libby, P. A., Bray, K. N. C., & Moss, J. B. (1979). Effects of finite reaction rate and molecular transport in premixed turbulent combustion. Combustion and Flame, 34, 285-301.

[17] Spalding, D. B. (1977). Development of the eddy-break-up model of turbulent combustion. Symposium (International) on Combustion, 16(1), 1657–1663. https://doi.org/10.1016/s0082-0784(77)80444-x

[18] K. N. C. Bray and P. A. Libby, "Passage Times and Flamelet Crossing Frequencies in Premixed Turbulent Combustion," Combustion Science and Technology, vol. 47, no. 5–6, pp. 253–274, Jun. 1986, doi: 10.1080/00102208608923877.

[19] Colin, O., Ducros, F., Veynante, D., & Poinsot, T. (2000). A thickened flame model for large eddy simulations of turbulent premixed combustion. Physics of fluids, 12(7), 1843-1863.

[20] Hawkes, E. R., & Cant, R. S. (2000). A flame surface density approach to large-eddy simulation of premixed turbulent combustion. Proceedings of the Combustion Institute, 28(1), 51-58.

[21] Chakraborty, N., & Swaminathan, N. (2007). Influence of the Damköhler number on turbulence-scalar interaction in premixed flames. I. Physical insight. Physics of Fluids, 19(4).

[22] Rasool, R., Chakraborty, N., & Klein, M. (2020). Algebraic flame surface density modelling of high pressure turbulent premixed Bunsen Flames. Flow, Turbulence and Combustion, 106(4), 1313–1327. https://doi.org/10.1007/s10494-020-00128-y

[23] Keil, F. B., Chakraborty, N., & Klein, M. (2020). Flame surface density transport statistics for high pressure turbulent premixed Bunsen Flames in the context of large eddy simulation. Combustion Science and Technology, 192(11), 2070–2092. https://doi.org/10.1080/00102202.2020.1789122

[24] Guerrero, J. (2022). Pressurized turbulent premixed CH4/H2/Air Flame validation using openfoam. AIP Advances, 12(7). https://doi.org/10.1063/5.0098715

[25] Kutkan, H., & Guerrero, J. (2021). Turbulent premixed flame modeling using the algebraic flame surface wrinkling model: A comparative study between openfoam and Ansys fluent. Fluids, 6(12), 462. https://doi.org/10.3390/fluids6120462

[26] Eckbreth, A. C. (1996). Laser diagnostics for combustion temperature and species. Gordon and Breach Publishers

[27] Y. Liu, J. Tan, M. Wan, L. Zhang, and X. Yao, “Quantitative Measurement of OH∗ and CH∗ Chemiluminescence in Jet Diffusion Flames,” ACS Omega, vol. 5, no. 26, pp. 15922–15930, Jul. 2020, doi: 10.1021/acsomega.0c01093.

[28] K. Souflas, “Experimental investigation of OH*/CH* ratio variations in turbulent, disk stabilized, lean propane-air flames with inlet mixture preheat and

stratification," Exp Therm Fluid Sci, vol. 136, Aug. 2022, doi: 10.1016/j.expthermflusci.2022.110670.

[29] Higgins, B., McQuay, M. Q., Lacas, F., & Candel, S. (2001). An experimental study on the effect of pressure and strain rate on CH chemiluminescence of premixed fuel-lean methane/Air Flames. Fuel, 80(11), 1583–1591. https://doi.org/10.1016/s0016-2361(01)00040-0

[30] Higgins, B., McQuay, M. Q., Lacas, F., Rolon, J. C., Darabiha, N., & Candel, S. (2001). Systematic measurements of oh chemiluminescence for fuel-lean, high-pressure, premixed, laminar flames. Fuel, 80(1), 67–74. https://doi.org/10.1016/s0016-2361(00)00069-7

[31] M. J. Bedard, T. L. Fuller, S. Sardeshmukh, and W. E. Anderson, "Chemiluminescence as a diagnostic in studying combustion instability in a practical combustor," Combust Flame, vol. 213, pp. 211–225, Mar. 2020, doi: 10.1016/j.combustflame.2019.11.039.

[32] Ashurst, W. T., Shepherd, I. G. (1997). Flame Front curvature distributions in a turbulent premixed flame zone. Combustion Science and Technology, 124(1–6), 115–144. https://doi.org/10.1080/00102209708935642

[33] Mokhtarian, F., & Mackworth, A. (1986). Scale-based description and recognition of planar curves and two-dimensional shapes. IEEE Transactions on Pattern Analysis and Machine Intelligence, PAMI-8(1), 34–43. https://doi.org/10.1109/tpami.1986.4767750

[34] Gülder, Ö. L., Smallwood, G. J., Wong, R., Snelling, D. R., Smith, R., Deschamps, B. M., & Sautet, J.-C. (2000). Flame front surface characteristics in turbulent premixed propane/air combustion. Combustion and Flame, 120(4), 407–416. https://doi.org/10.1016/s0010-2180(99)00099-1

[35] Thiesset, F., Halter, F., Bariki, C., Lapeyre, C., Chauveau, C., Gökalp, I., Selle, L., & Poinsot, T. (2017). Isolating strain and curvature effects in premixed

flame/vortex interactions. Journal of Fluid Mechanics, 831, 618–654. https://doi.org/10.1017/jfm.2017.641

[36] Zheng, Y., Weller, L., & Hochgreb, S. (2022). Instantaneous flame front identification by mie scattering vs. oh plif in low turbulence Bunsen Flame. Experiments in Fluids, 63(5). https://doi.org/10.1007/s00348-022-03423-8

[37] Wang, X., Cheng, X., Lu, H., Pan, F., Qin, L., & Wang, Z. (2020). Effect of burner diameter on structure and instability of turbulent premixed flames. Fuel, 271, 117545. https://doi.org/10.1016/j.fuel.2020.117545

[38] Troiani, G., Lapenna, P. E., Lamioni, R., & Creta, F. (2022). Self-wrinkling induced by Darrieus-Landau instability in turbulent premixed Bunsen Flames from low to moderately high Reynolds numbers. Physical Review Fluids, 7(5). https://doi.org/10.1103/physrevfluids.7.053202

[39] Zhang, W., Wang, J., Guo, S., Yu, Q., Jin, W., Zhang, M., & Huang, Z. (2019). Effects of integral scale on darrieus–landau instability in turbulent premixed flames. Flow, Turbulence and Combustion, 103(1), 225–246. https://doi.org/10.1007/s10494-018-0006-4

[40] Zhang, M., Chang, M., Wang, J., & Huang, Z. (2020). Flame dynamics analysis of highly hydrogen-enrichment premixed turbulent combustion. International Journal of Hydrogen Energy, 45(1), 1072–1083. https://doi.org/10.1016/j.ijhydene.2019.10.194

[41] Zhang, W., Wang, J., Lin, W., Li, G., Hu, Z., Zhang, M., & Huang, Z. (2021). Effect of hydrogen enrichment on flame broadening of turbulent premixed flames in thin reaction regime. International Journal of Hydrogen Energy, 46(1), 1210–1218. https://doi.org/10.1016/j.ijhydene.2020.09.159

[42]Zheng, Y., Weller, L., & Hochgreb, S. (2023). 3D flame surface density measurements via orthogonal cross-planar mie scattering in a low-turbulence Bunsen Flame. Proceedings of the Combustion Institute, 39(2), 2369–2377. https://doi.org/10.1016/j.proci.2022.07.076

[43] Tyagi, A., & O'Connor, J. (2020). Towards a method of estimating out-of-plane effects on measurements of turbulent Flame Dynamics. Combustion and Flame, 216, 206–222. https://doi.org/10.1016/j.combustflame.2020.02.010

[44] Ayoola, B. O., Balachandran, R., Frank, J. H., Mastorakos, E., & Kaminski, C. F. (2006). Spatially resolved heat release rate measurements in turbulent premixed flames. Combustion and Flame, 144(1–2), 1–16. https://doi.org/10.1016/j.combustflame.2005.06.005

[45] Lauer, M., Sattelmayer, T. (2009). On the adequacy of chemiluminescence as a measure for heat release in turbulent flames with mixture gradients. Volume 2: Combustion, Fuels and Emissions. https://doi.org/10.1115/gt2009-59631

[46] Bouvet, N., Chauveau, C., Gökalp, I., Lee, S.-Y., & Santoro, R. J. (2011). Characterization of syngas laminar flames using the Bunsen burner configuration. International Journal of Hydrogen Energy, 36(1), 992–1005. https://doi.org/10.1016/j.ijhydene.2010.08.147

[47] Halter, F., Chauveau, C., Gokalp, I. (2007). Characterization of the effects of hydrogen addition in premixed methane/Air Flames. International Journal of Hydrogen Energy, 32(13), 2585–2592 https://doi.org/10.1016/j.ijhydene.2006.11.033

[48] Favre, A. J. (1965). The Equations of Compressible Turbulent Gases. https://doi.org/10.21236/ad0622097

[49] David G. Goodwin, Harry K. Moffat, Ingmar Schoegl, Raymond L. Speth, and Bryan W. Weber. Cantera: An object-oriented software toolkit for chemical kinetics, thermodynamics, and transport processes. https://www.cantera.org, 2022. Version 2.6.0. doi:10.5281/zenodo.6387882

[50] Pope, S. B. (2004). Ten questions concerning the large-eddy simulation of turbulent flows. New Journal of Physics, 6, 35–35. https://doi.org/10.1088/1367-2630/6/1/035

[51] Weller, H. G., Tabor, G., Jasak, H., & Fureby, C. (1998). A tensorial approach to computational continuum mechanics using object-oriented techniques. Computers in Physics, 12(6), 620–631. https://doi.org/10.1063/1.168744

[52] Weller, H. G., Tabor, G., Gosman, A. D., & Fureby, C. (1998). Application of a flame-wrinkling Les Combustion model to a turbulent mixing layer. Symposium (International) on Combustion, 27(1), 899–907. https://doi.org/10.1016/s0082-0784(98)80487-6

[53] Gülder, Ömer L. (1991). Turbulent premixed flame propagation models for different combustion regimes. Symposium (International) on Combustion, 23(1), 743–750. https://doi.org/10.1016/s0082-0784(06)80325-5

[54] Kee, R. J. (1993). A Fortran Chemical Kinetics Package for the Analysis of Gas Phase Chemical Kinetics. SANDIA REPORT, SAND89-8009B, UC-706.

[55] A. Burcat and B. Ruscic, “Third Millennium Ideal Gas and Condensed Phase Thermochemical Database for Combustion with updates from Active Thermochemical Tables,” Sep. 2005

[56] Dinkelacker, F., Manickam, B., & Muppala, S. P. R. (2011). Modelling and simulation of lean premixed turbulent methane/hydrogen/air flames with an effective Lewis number approach. Combustion and Flame, 158(9), 1742-1749.

[57] Killer C, “Abel Inversion Algorithm.” MATLAB Central File Exchange, 2023. [Online]. Available: Abel Inversion Algorithm (https://www.mathworks.com/matlabcentral/fileexchange/43639-abel-inversion-algorithm)

[58] Pretzier, G. (1991). A new method for Numerical Abel-Inversion. Zeitschrift Für Naturforschung A, 46(7), 639–641. https://doi.org/10.1515/zna-1991-0715

[59] D’Amato, A. (2018). Development of an Abel Transform Algorithm for Combustion Characterization and Data Analysis (thesis).

[60] Kobayashi, H., Tamura, T., Maruta, K., Niioka, T., & Williams, F. A. (1996). Burning velocity of turbulent premixed flames in a high-pressure environment. Symposium (International) on Combustion, 26(1), 389–396. https://doi.org/10.1016/s0082-0784(96)80240-2

[61] Ranganathan, S., Petrow, D., Rockwell, S. R., & Rangwala, A. S. (2018). Turbulent burning velocity of methane–air–dust premixed flames. Combustion and Flame, 188, 367–375. https://doi.org/10.1016/j.combustflame.2017.10.015

[62] Domingo, P., & Vervisch, L. (2022). Revisiting the relation between premixed flame brush thickness and turbulent burning velocities from Ken Bray's notes. Combustion and Flame, 239, 111706.

[63] Attili, A., Luca, S., Denker, D., Bisetti, F., & Pitsch, H. (2021). Turbulent flame speed and reaction layer thickening in premixed jet flames at constant Karlovitz and increasing Reynolds numbers. Proceedings of the Combustion Institute, 38(2), 2939-2947.

APPENDICES

A. MATLAB Code for Abel Transform

```
close all;
clear all;
clc;
clearvars;
format long g;
format compact;

image_variable1=imread('G:\Dilay\Matlab Averages\OH\06-20H2-OH-v.bmp');
background_im=imread('G:\Dilay\Matlab Averages\OH\background\06-20H2-OH-
bg.bmp');
subtracted_image=image_variable1-background_im;
imshow(subtracted_image)
title('Original Image')
C=imcrop(subtracted_image, [0 0 788 580] ); %removed text part of the
fig.
I=rgb2gray(C);
imadjust(I);
imshow(I)
%Detect Flame Edges with Sobel Filter and find the flame center using
%weighted centeroids on the intensity figure
edge_detected=edge(I,'sobel');
BW=bwperim(imfill(imdilate(imdilate(edge_detected,strel('line',2,0)), ...
    strel('line',2,90)),'holes'));
imshow(BW)
s = regionprops(BW,I,{'WeightedCentroid'});
title('Weighted Centroids');
hold on
numObj = numel(s);
for k = 1 : numObj
    plot(s(k).WeightedCentroid(1), s(k).WeightedCentroid(2), 'r*');
end
hold off
%Crop the pilot flame area to reduce its effect on flame shape.
D=imcrop(subtracted_image, [514 0 788 580] );
figure(1)
I=rgb2gray(D);
I=imnlmfilt(I);
I=medfilt2(I);
I=imadjust(I);
I=medfilt2(I);
imshow(I)
title('Half Image')
savefig('BWHalf06-20H-OH.fig') %only for demonstration purposes
% Save the figure to specified location with specified name
folder_path = 'G:\Dilay\Abel Inversion\0.6\20H2\OH';
file_name = 'HalfImage.png';
```

```
file_path = fullfile(folder_path, file_name);
saveas(gcf, file_path, 'png');

%Center the flame image according to the flame center found from weighted
%centeroids, and save the figure in both png and .fig formats in
% grayscale for later postprocessing
E=imcrop(subtracted_image, [240 0 788 580] );
figure(2)
I=rgb2gray(E);
I=imnlmfilt(I);
I=medfilt2(I);
I=imadjust(I);
I=medfilt2(I);
imshow(I)
title('Black and White Image')
set(gca, 'FontSize', 16, 'FontWeight', 'bold')
savefig('BW06-20H-OH.fig')
folder_path = ['G:\Dilay\Abel Inversion\0.6\20H2\OH'];
file_name = 'BWImage.png';
file_path = fullfile(folder_path, file_name);
set(gcf, 'PaperPosition', [0 0 20 20]);
saveas(gcf, file_path, 'png');

%Finding the Intensity Graph
%This part of the code is used to calculate the intensity graph of the
%flame image. The intensity data is stored in x-y-z coordinates, where
the
%z coordinate corresponds to the intensity value. At this stage, the code
%does not perform any normalization procedure to avoid data loss.
open (['G:\Dilay\Abel Inversion\BW06-20H-OH.fig']);
rad_fit = gcf;
axesObjs = get(rad_fit, 'Children');
dataObjs = get(axesObjs, 'Children');
xdata = get(dataObjs, 'XData');
ydata = get(dataObjs, 'YData');
cdata = get(dataObjs, 'CData');
x=linspace(0,100, xdata(end));
y=linspace(0,127, ydata(end));
cdata=flipud(cdata);
[X,Y]=meshgrid(x,y);
figure(3)
surf(X,Y,cdata)
view([0 0 1])
colormap(jet)
xlabel('x [mm]')
ylabel('y [mm]')
shading interp
lighting flat
axis equal
axis ([0 100 0 100])
xticks([0 10 20 30 40 50 60 70 80 90 100 110 120 130 140 150])
yticks([0 10 20 30 40 50 60 70 80 90 100 110 120 130 140 150])
title('Intensity')
```

```
set(gca, 'FontSize', 16, 'FontWeight', 'bold')
%Save the postprocessed image
folder_path = 'G:\Dilay\Abel Inversion\0.6\20H2\OH';
file_name = 'Intensity.png';
file_path = fullfile(folder_path, file_name);
set(gcf, 'PaperPosition', [0 0 20 20]);
saveas(gcf, file_path, 'png');
close(figure)
%End of Intensity Graph part.

%Combining the intensity values to create a vertically averaged flame
%shape, the new image includes only the right hand size of the figure.
The
%RHS is later used to create a symmetric image.
i_center=cdata(:,290);
i_right=cdata(:,290:end);
i_left=cdata(:,1:291);

% The new image includes only the RHS x coordinates of the intensity
% values (xNew), and the radial positions of the RHS of the image (r)
xNew = horzcat(i_center, i_right);
r = linspace(0, 50, length(xNew(1,:)));
% Plot the Original Half image
figure(5)
[R,Y2] = meshgrid(r, y);
surf(R, Y2, xNew);
view([0 0 1])
colormap(jet)
xlabel('r [mm]')
ylabel('z [mm]')
shading interp
axis equal
axis([0 50 0 100])
yticks([0 10 20 30 40 50 60 70 80 90 100])
xticks([0 10 20 30 40 50])
title ('Original Image')
set(gca, 'FontSize', 16, 'FontWeight', 'bold')
% Save image
folder_path = 'G:\Dilay\Abel Inversion\0.6\20H2\OH';
file_name = 'OriginalImage.png';
file_path = fullfile(folder_path, file_name);
set(gcf, 'PaperPosition', [0 0 20 20]);
saveas(gcf, file_path, 'png');

%The Pretzier Procedure is employed to calculate the Abel transform.
% Fourier Expansion is used to calculate Pretzier procedure.
R3=50.0001; %Half value of the window
lof=1;
upf=40;
%fnCos:cosine functions set
% rows=x-values (radial values)
% columns= number of expansion elements, start with n=0, number is equal
to
```

```
% n+1
fnCos=zeros(length(r),upf+1);
%fnAbel:Direct Abel transformation applied to fnCos
fnAbel=zeros(length(r),upf+1);
%calculate fnCos and fnAbel
fnCos(:,1)=1;
for c=1:length(r);
    yy=r(c);
    funM = @(t) 2.*t./sqrt(t.^2-yy.^2);
    fnAbel(c,1) = integral(funM,yy,R3);
end
% 2. all other expansion numbers (a.k.a. all other columns)
for n=1:upf
    for c=1:length(r)
        yy=r(c);
        fnCos(c,n+1)=(1-(-1)^n*cos(n*pi*yy/R3));
        funM = @(t) 2.*(1- (-1)^n*cos(n*pi.*t/R3)).*t./sqrt(t.^2-yy.^2);
        fnAbel(c,n+1)= integral(funM,yy,R3);
    end
end

%Replace the real data with the transformed/projected data
% f_Intensity: radial intensity distribution matrix
f_Intensity=zeros(length(r),length(y));
% AM matrix: unknown amplitude
%AM = BM * inv(CM)
AM=zeros(length(y),upf+1);
BM = zeros(length(y),upf+1);
CM= zeros(upf+1,upf+1);
xNew=double(xNew);
for j=1:length(y)
    for k=1:upf+1
        for l=1:upf+1
            CM(l,k)=sum(fnAbel(:,k).*fnAbel(:,l));
        end
        BM(j,k)= sum(xNew(j,:)'.*fnAbel(:,k));
    end
     AM(j,:)=BM(j,:)*inv(CM);
end
%Calculation of the radial distribution
for j=1:length(y)
    f_Intensity(:,j)=f_Intensity(:,j)+AM(j,1)*1;
    for a = 2:upf+1
        f_Intensity(:,j)=f_Intensity(:,j)+AM(j,a).*fnCos(:,a);
    end
end
%Direct Abel Transform
% Application of direct Abel transform to the radial distribution to
% calculate the projection and compare with initial image
% Allocation of radius vector and radial distribution
mesh = length(r);
for j=1:length(y)
    for i=1:mesh
```

```
        rad_location(i,j)=r(1,i);
        intensity_value(i,j)=f_Intensity(i,j);
    end
end
%interpolate the radial distribution at each station alonf the flame axis
ord=2; %interpolation order initial choice
for j=1:length(y)
    rad_fit=polyfit(rad_location(:,j),intensity_value(:,j),ord);
    rad_poly(:,j)=polyval(rad_fit,r); %interpolating polynomial valued at
each radius
end
%increase the interpolation order by means of while cycle assuring that
the
%relative error between the interolating polynomial and the radial
%distribution is below a certain value
for j=length(y)
    ord=2;
    while abs(max(rad_poly(:,j)-
f_Intensity(:,j))./max(f_Intensity(:,j)))>0.1
        ord = ord+1;
        rad_fit=polyfit(rad_location(:,j),intensity_value(:,j),ord);
        rad_poly(:,j)=polyval(rad_fit,r);
    end
    %create a continuing function by means of interpolating polynomial
    % i.o.t. apply the direct abel transform.
        holder1=@(t,i) t.^i;
        holder_sum=@(t) rad_fit(end).*t.^0;
        ss=ord;
        for i=1:ord
            holder_func=@(t) rad_fit(i)*holder1(t,ss);
            holder_sum=@(t) holder_sum(t)+holder_func(t);
            ss=ss-1;
        end
        for i=1:length(r)
            holder_r=r(i);
            f=@(t) 2.*holder_sum(t).*t./sqrt(t.^2 - holder_r^2);
%function in the
            % abel integral
            project(i,j)= integral(f,holder_r,R3);
            %direct abel transform i.o.t. have the projection
        end
end
f_Intensity_Abel=(f_Intensity);
%Radial distribution
f_Intensity_Abel(f_Intensity_Abel <0) = 1e-20;
figure(6)
surf(y,r,f_Intensity_Abel)
view([1 0 -1])
colormap(jet)
xlabel('axial [mm]')
ylabel('radial [mm]')
shading interp
axis equal
```

```
axis ([0 100 0 50])
xticks([0 10 20 30 40 50 60 70 80 90 100 110])
yticks([0 10 20 30 40 50])
shading interp
title('Radial Distribution')
set(gca, 'FontSize', 16, 'FontWeight', 'bold')
% Save figure
folder_path = 'G:\Dilay\Abel Inversion\0.6\20H2\OH';
file_name = 'RadialDistribution.png';
file_path = fullfile(folder_path, file_name);
set(gcf, 'PaperPosition', [0 0 20 20]);
saveas(gcf, file_path, 'png');

%Normalization Part (normalize by the maximum value
figure(7)
fnorm=f_Intensity_Abel/max(f_Intensity_Abel(:));
hand = surf(y,r,fnorm)
set(hand, 'XData', -1*get(hand,'XData'));
surf(y,r,fnorm)
colormap(jet)
xlabel('axial [mm]')
ylabel('          radial [mm]','HorizontalAlignment', 'center')
shading interp
axis equal
axis ([0 100 0 50])
xticks([0 10 20 30 40 50 60 70 80 90 100 110])
yticks([0 10 20 30 40 50])
view([1 0 -1])
clim([0 1])
title('Normalized Radial Distribution')
set(gca, 'FontSize', 16, 'FontWeight', 'bold')
% Save figure
folder_path = 'G:\Dilay\Abel Inversion\0.6\20H2\OH';
file_name = 'NormalizedRD.png';
file_path = fullfile(folder_path, file_name);
set(gcf, 'PaperPosition', [0 0 20 20]);
saveas(gcf, file_path, 'png');
```

B. Matlab Code for Curvature and PDF of Mie Scattering Data

```
clc;
clearvars;
close all;

% Load the binary flame image
flame_image =
imread('/Users/dilayguleryuz/Documents/Thesis/Experiment/Mie-
Example/ER06-0H2-SEG.bmp');
imshow(flame_image)
flame_image = bwareaopen(flame_image, 1000);
flame_image = imcrop(flame_image, [0 0 118 250]);
flame_image(end,:) = 0;
% Remove any singleton dimensions
flame_image = squeeze(flame_image);
imshow(flame_image)
% Extract the boundary coordinates of the flame contour
boundaries = bwboundaries(flame_image);

% Extract the coordinates of the first boundary
boundary = boundaries{1};
x = boundary(:, 2);
y = boundary(:, 1);


% Fit a B-spline curve to the boundary
num_points = 1000;
t = linspace(0, 1, length(x));
tq = linspace(0, 1, num_points);
xq = spline(t, x, tq);
yq = spline(t, y, tq);

% Plot the original boundary and the B-spline curve
figure
imshow(flame_image)
hold on
plot(x, y, 'r', 'LineWidth',2)
plot(xq, yq, 'g', 'LineWidth',3)
legend('Original boundary', 'B-spline curve')
title('Flame contour analysis')

% Interpolate a curve between the original boundary points
num_points = 1000;
tq = linspace(0, 1, num_points);
ti = linspace(0, 1, length(x));
xi = interp1(ti, x, tq, 'spline');
yi = interp1(ti, y, tq, 'spline');

% Calculate the distances between adjacent points on the curve
distances = sqrt(diff(xi).^2 + diff(yi).^2);
```

```
% Specify the desired distance between adjacent points
A = 2;

% Resample the curve at fixed distances
tq = [0 cumsum(distances)/A];
xq = interp1(tq, xi, linspace(0, max(tq), num_points), 'spline');
yq = interp1(tq, yi, linspace(0, max(tq), num_points), 'spline');

% Plot the original boundary and the resampled curve
figure
imshow(flame_image)
hold on
plot(x, y, 'r', 'LineWidth',2)
plot(xq, yq, 'g', 'LineWidth',3)
legend('Original boundary', 'Resampled curve')
title('Flame contour analysis')

% Interpolate a curve between the original boundary points
num_points = 1000;
tq = linspace(0, 1, num_points);
ti = linspace(0, 1, length(x));
xi = interp1(ti, x, tq, 'spline');
yi = interp1(ti, y, tq, 'spline');

% Calculate the distances between adjacent points on the curve
distances = sqrt(diff(xi).^2 + diff(yi).^2);

% Specify the desired distance between adjacent points
A = 5;

% Resample the curve at fixed distances
tq = [0 cumsum(distances)/A];
xq = interp1(tq, xi, linspace(0, max(tq), num_points), 'spline');
yq = interp1(tq, yi, linspace(0, max(tq), num_points), 'spline');

% Plot the original boundary and the resampled curve
figure
imshow(flame_image)
hold on
plot(x, y, 'r', 'LineWidth',2)
plot(xq, yq, '-s', 'Color', 'g', 'LineWidth', 2, 'MarkerSize', 5,
'MarkerEdgeColor', 'blue')
legend('Original boundary', 'Resampled curve')
title('Flame contour analysis')

%CIRCLE PART
% Initialize the matrix to store circle radii
radii = zeros(1, length(xq)-2);

% Fit circles to every 3 consecutive points
for i = 1:length(xq)-2
% Get the coordinates of the 3 points
x1 = xq(i);
```

```
y1 = yq(i);
x2 = xq(i+1);
y2 = yq(i+1);
x3 = xq(i+2);
y3 = yq(i+2);

% Calculate the center and radius of the circle passing through the 3
points
A = [x1-x2 y1-y2; x1-x3 y1-y3];
b = [0.5*(x1^2-x2^2+y1^2-y2^2); 0.5*(x1^2-x3^2+y1^2-y3^2)];
center = A\b;
radius = sqrt((x1-center(1))^2 + (y1-center(2))^2);

% Store the radius in the matrix
radii(i) = radius;

% Plot the circle
theta = linspace(0, 2*pi, 100);
x_circle = center(1) + radius*cos(theta);
y_circle = center(2) + radius*sin(theta);
% plot(x_circle, y_circle, 'm', 'LineWidth', 2);
end

% Display the radii matrix
%disp(radii);
% % % Define function to calculate curvature of a circle with radius r
% % curvature_from_radius = @(r) 1 / r;

% Initialize matrix to store curvature values
curvature_matrix = zeros(length(xq), 1);

% Loop over resampled curve points
for i = 2:length(xq)-1
    % Get 3 consecutive points
    x1 = xq(i-1);
    y1 = yq(i-1);
    x2 = xq(i);
    y2 = yq(i);
    x3 = xq(i+1);
    y3 = yq(i+1);
    % Calculate the vectors formed by the 3 points
    v1 = [x1 - x2, y1 - y2];
    v2 = [x3 - x2, y3 - y2];
    % Calculate the cross product of the vectors
    cross_product = v1(1) * v2(2) - v1(2) * v2(1);
    % Determine the sign of the curvature based on the cross product
    if cross_product > 0
        sign = 1;   % curve is concave up
    elseif cross_product < 0
        sign = -1;  % curve is concave down
    else
        sign = 0;   % curvature is 0
    end
```

```
    % Calculate the radius and curvature
    distance = norm(v1);
    radius = distance / (2 * abs(cross_product));
    curvature = sign / radius;
    % Store curvature value in matrix
    curvature_matrix(i) = curvature;
end

% Define the range of values over which to estimate the PDF
x = linspace(-2, 2, 100);
% Estimate the PDF using the built-in 'pdf' function
curvature_pdf = pdf('Normal', x, mean(curvature_matrix),
std(curvature_matrix));
% Normalize PDF to integrate to 1
bin_width = x(2) - x(1);
curvature_pdf = curvature_pdf / (bin_width * sum(curvature_pdf));
figure(5)
% Plot the PDF
plot(x, curvature_pdf);
xlabel('Curvature');
ylabel('Probability Density');
title('PDF of Curvature Matrix');

function [xc, yc, R] = circfit(x, y)
    % Compute the moments of the point set
    N = length(x);
    x_mean = mean(x);
    y_mean = mean(y);
    u = x - x_mean;
    v = y - y_mean;
    Suu = sum(u.^2);
    Suv = sum(u.*v);
    Svv = sum(v.^2);
    Suuu = sum(u.^3);
    Suvv = sum(u.*v.^2);
    Svvv = sum(v.^3);

    % Solve the linear system of equations to obtain the circle center
    A = [Suu, Suv; Suv, Svv];
    b = [0.5*Suuu + 0.5*Suvv; 0.5*Svvv + 0.5*Suvv];
    sol = A \ b;
    xc = sol(1) + x_mean;
    yc = sol(2) + y_mean;
    % Compute the circle radius
    R = sqrt((x-xc).^2 + (y-yc).^2);
    R = mean(R);
end
```